Biomaterials Science

ROYAL SOCIETY OF CHEMISTRY

PAPER

View Article Online
View Journal | View Issue

Cite this: *Biomater. Sci.*, 2022, **10**, 3201

Targeted delivery of irinotecan and SLP2 shRNA with GRP-conjugated magnetic graphene oxide for glioblastoma treatment

Chi-Cheng Chuang,†[a,b] Yu-Hsiang Lan,†[b] Yu-Jen Lu,†[a,b] Yu-Lun Weng[c] and Jyh-Ping Chen *[a,c,d,e,f]

Received 22nd March 2022,
Accepted 26th April 2022

DOI: 10.1039/d2bm00420h

rsc.li/biomaterials-science

Magnetic nanoparticles (MNPs) are useful for magnetic targeted drug delivery while ligand-mediated active targeting is another common delivery strategy for cancer therapy. In this work, we intend to prepare magnetic graphene oxide (mGO) by chemical co-precipitation of MNPs on the GO surface, followed by conjugation of the gastrin releasing peptide (GRP) as a targeting ligand, for dual targeted drug/gene delivery in invasive brain glioma treatment. mGO was grafted with chitosan, complexed with shRNA plasmid DNA for stomatin-like protein 2 (SLP2) gene silencing, modified with urocanic acid for plasmid DNA endosomal escape, PEGylated for GRP conjugation, and loaded with the chemotherapeutic drug irinotecan (CPT-11) by $\pi-\pi$ interaction for pH-responsive drug release (mGOCUG/CPT-11/shRNA). In addition to the in depth characterization of the physico–chemical and biological properties during each preparation step, we also study the loading/pH-responsive release behavior of CPT-11 and the shRNA plasmid loading/cell transfection efficiency. The targeting and antitumor efficacies of the nanocomposite were studied with U87 human glioblastoma cells *in vitro*. An *in vivo* study revealed that intravenous administration followed by magnetic guidance results in the efficient targeted delivery of mGOCUG/CPT-11/shRNA to orthotopic brain tumors in nude mice, and it exhibits excellent antitumor efficacy with a reduced tumor growth rate and prolonged animal survival time. Our work thus highlights a multifunctional mGO-based drug/gene delivery platform for effective combination cancer therapy in glioblastoma treatment.

1. Introduction

Glioblastoma multiforme (GBM), or grade IV glioma, remains the most aggressive type of primary brain tumor, accounting for nearly 70% of all malignant gliomas. Currently, there are no curative treatment options for GBM and the prognosis is often bleak, with the median survival time ranging from 12 to 15 months and a 5-year survival rate of 6.8%.[1,2] Increasing evidence has elucidated a positive relationship between surgical resection and survival.[3,4] However, complete resection of GBM is not possible due to its highly infiltrative and invasive nature.[5] Therefore, chemotherapy and radiotherapy play a crucial role in current treatment modalities to prevent recurrence.[6] Irinotecan (CPT-11), a chemotherapeutic drug sold under the brand name Camptosar®, is found to be effective in treating GBM by inhibiting the DNA eukaryotic enzyme topoisomerase I.[7,8] Nonetheless, the major hurdle hindering the successful use of chemotherapy could be the intolerable adverse side effects imposed on patients. These cytotoxic agents usually lack a specific targeting ability to differentiate between normal and malignant cells, leading to devastating effects on healthy brain tissue while killing cancer cells minimally. Therefore, the restrictions inherent in conventional brain cancer therapy encourage the development of an innovative targeting strategy with enhanced selectivity toward cancer cells while avoiding toxic side effects with minimum influence on non-disease sites.

Nano-sized drug carriers have been attracting tremendous interest due to their potential use as tumor-selective drug delivery vehicles, owing to their characteristic features of

[a]*Department of Neurosurgery, Chang Gung Memorial Hospital, Linkou, Kwei-San, Taoyuan 33305, Taiwan. E-mail: jpchen@mail.cgu.edu.tw*
[b]*College of Medicine, Chang Gung University, Taoyuan 33305, Taiwan*
[c]*Department of Chemical and Materials Engineering, Chang Gung University, Taoyuan 33305, Taiwan*
[d]*Department of Plastic and Reconstructive Surgery and Craniofacial Research Center, Chang Gung Memorial Hospital, Linkou, Kwei-San, Taoyuan 33305, Taiwan*
[e]*Research Center for Food and Cosmetic Safety, College of Human Ecology, Chang Gung University of Science and Technology, Taoyuan 33302, Taiwan*
[f]*Department of Materials Engineering, Ming Chi University of Technology, Tai-Shan, New Taipei City 24301, Taiwan*
†These authors contributed equally to this paper.

loading a sufficient amount of drugs within themselves while releasing the desirable amount of drugs in the right place.[9,10] In addition, tumor vessels are typically leaky with large endothelial interstitial gap junctions of about 100 nm.[11] Nanomaterials can therefore reach tumors *via* the enhanced permeability and retention (EPR) effect.[12] Among the nanocarriers for drug delivery, graphene oxide (GO) is frequently used due to its advantages such as a large surface area, biocompatibility, a two-dimensional planar structure, and chemical and mechanical stability.[13] Moreover, π–π stacking between therapeutic drugs and GO allows high-efficiency loading and controlled release of anticancer drugs.[14] Indeed, an added advantage of GO for drug delivery will be its pH-responsive drug release behavior, which will lead to efficient intracellular release of therapeutic agents in an acidic endosomal environment, following the endocytosis of drug-loaded GO by cancer cells.[15] Interestingly, for drug delivery to the brain, graphene nanostructures (including GO, reduced GO and graphene quantum dots) showed a potential ability to cross the blood–brain barrier (BBB) in targeted drug delivery systems, making GO a potential candidate for glioblastoma treatment.[16] Nonetheless, there are still some limitations existing in nanocarrier-based drug delivery systems. Nanocarriers may undergo rapid elimination from the reticuloendothelial (RES) system due to their small size,[17] while still lacking "smart" selectivity for tumor tissues.[18]

In recent years, iron oxide (Fe_3O_4) magnetic nanoparticles (MNPs) have been widely used for targeted drug/gene delivery, owing to their excellent superparamagnetic properties, biocompatibility, low cytotoxicity, biodegradability and reactive surface that can be readily modified with desirable moieties.[19] Since MNPs can be driven to a specific site by a strong permanent gradient magnetic field, magnetic targeting with these MNPs may serve as a feasible strategy for the delivery of chemotherapeutic agents to the targeted tumor site.[20,21] Conjugating a nanocarrier with ligand molecules that could specifically bind to overexpressed receptors on the cancer cell surface is another common strategy for active targeted drug delivery in cancer therapy.[22] The gastrin-releasing peptide receptor (GRPR), a G protein-coupled receptor, has emerged recently as an potential targeted moiety in cancer therapy, due to its overexpression in numerous human tumors, including glioblastoma,[23] small cell lung cancer,[24] cervical cancer,[25] head/neck squamous cell cancer,[26] colon cancer,[27] breast cancer[28] and prostate cancer.[29] Furthermore, GRPR expression is more commonly found in malignancies than in normal tissues.[30] Therefore, modifying drug-loaded nanocarriers with the gastrin-releasing peptide (GRP), a mammalian bombesin-like peptide with high binding affinity to the GRPR, is expected to enhance their intracellular uptake by GRPR-expressing cancer cells through ligand-mediated targeted drug delivery, and therefore increase the drug concentration in the targeted area.[31] Toward this end, we aim to augment this active targeting mechanism with magnetic targeting by developing a magnetic GO-based nanocarrier for CPT-11 loading, *via* chemical co-precipitation of Fe_3O_4 MNPs on the GO surface, which is expected to be precisely driven to tumors using an external magnetic field as well as equipped with a GRP targeting ligand to enhance intracellular uptake by tumor cells.

On the other hand, single drug chemotherapy might not be capable of efficiently eradicating all malignant cells because of the development of drug resistance to chemotherapeutic drugs. Resistant cells adopt mechanisms to evade the apoptotic pathways induced by these cytotoxic agents.[32] Other limiting factors that hamper the effectiveness of chemotherapy include the tumor heterogeneity or the existence of cancer cells at different cell division or growth stages.[33] Hence, combination therapy using distinct molecular targets can lead to improved treatment outcomes by preventing the development of drug resistance.[34] Furthermore, studies revealed that combined gene therapy and chemotherapy exerts synergistic antitumor efficacy.[35,36] Specifically, the co-delivery of drugs and plasmid DNA has become an increasingly important strategy for enhanced anti-cancer effects in combination cancer therapy.[37]

RNA interference (RNAi) using small interfering RNA (siRNA) is a novel therapeutic strategy for GBM, which is based on the highly specific and efficient silencing of target genes involved in tumor cell proliferation, metastasis, invasion, and angiogenesis.[38] However, the successful delivery of naked siRNA into the cytoplasm of the targeted cells to exert its RNAi function is challenging. Firstly, circulating siRNA could be rapidly degraded by endonuclease in the serum even before reaching the targeted tissues with a half-life of only 15 min.[39] Secondly, naked siRNA does not freely cross the cell membrane owing to its anionic nature and large molecular weight. Thus, efficient intracellular delivery of siRNA requires suitable carriers to conquer these obstacles, including poor intracellular uptake and limited biological stability. Among non-viral delivery vectors, the use of chitosan is attractive, since it possesses beneficial qualities such as biocompatibility, biodegradability, low cytotoxicity and highly cationic polyelectrolyte nature.[40] Indeed, due to the presence of a vast amount of amino groups in its polymeric chain, chitosan carries a strong positive surface charge, which makes it suitable to bind and package highly negatively charged nucleotides such as siRNA for RNAi purpose.[41,42] Nonetheless, the molecular weight and degree of deacetylation of chitosan influence the silencing efficiency *in vitro*, as well as biodistribution and hemocompatibility *in vivo*.[43] Chitosan with a higher degree of deacetylation shows a higher capacity of gene complexation and a value higher than 65% (or 80%) is required for carrying plasmid DNA (or siRNA).[44] Chitosan with a high molecular weight is preferred to deliver the genetic material by providing better protection in the endosomes/lysosomes, but the stronger binding may restrict the release of gene materials.[45] The optimal chitosan molecular weight range for siRNA delivery was reported to be within the range of 60 to 160 kDa.[43]

To increase the siRNA transfection efficiency, imidazole group-containing urocanic acid can be used to modify chitosan to increase the release of complexed siRNA (plasmid DNA) into the cytoplasm.[46] By inducing the influx of water and ions

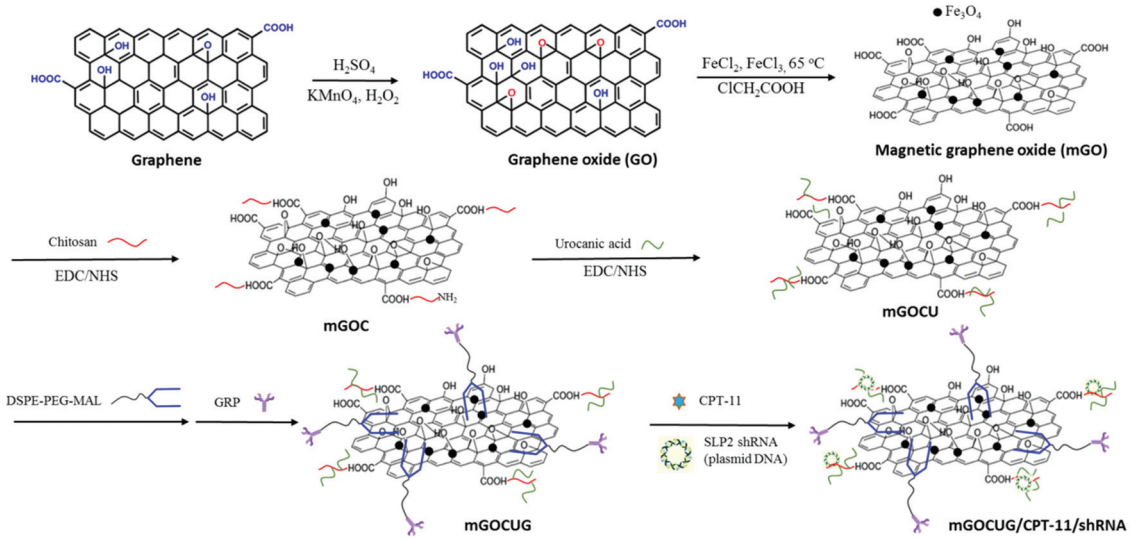

Fig. 1 The flow diagram for preparing CPT-11/SLP2 shRNA co-loaded, GRP-conjugated, and urocanic acid/chitosan-grafted magnetic graphene oxide. The size of Fe_3O_4 nanoparticles was not drawn to scale for better representation of the structure of graphene oxide.

into endosomes, the well-known proton sponge effect from urocanic acid will cause the rupture of endosomes/lysosomes and trigger the release of complexed siRNA (plasmid DNA) after its endocytosis to increase the cell transfection efficiency.[47]

Understanding the precise molecular mechanisms that mediate the regulation of glioma invasiveness would be of great clinical value since the major factor contributing to the bleak prognosis of GBM is the infiltrative behavior of glioma cells, leading to incomplete surgical resection and high recurrence rates.[48] Stomatin-like protein 2 (SLP2 or STOML2), a member of the stomatin superfamily, has been reported to be overexpressed in numerous human cancer tissues including glioma and is involved in tumor progression and occurrence.[49,50] Moreover, the up-regulation of SLP2 was significantly correlated with the World Health Organization (WHO) histological grade of gliomas and the overall survival time of patients suffered from this disease.[51] The invasive and migration ability of glioma cells was remarkably reduced by SLP2 gene silencing through inhibition of the nuclear factor κB/matrix metalloproteinase-9 (NF-κB/MMP9) pathway.[48] Depletion of SLP2 was also associated with enhanced sensitivity of cancer cells to chemotherapeutics-induced apoptosis.[48] Taken together, considering that SLP2 plays an oncogenic role in glioma progression and pathogenesis, the inhibition of SLP2 protein synthesis by RNAi may be a promising therapeutic strategy in glioblastoma treatment.

In this study, we aim to develop a co-delivery strategy of CPT-11 and SLP2 short hairpin RNA (shRNA) *via* dual-targeted nanoparticles, by combining magnetic targeting with ligand-mediated active targeting for the treatment of GBM. The magnetic graphene oxide (mGO) nanocarrier is conjugated with chitosan/urocanic acid (mGOCU) for shRNA complexation/endosomal escape. After PEGylation by interaction of the hydrophobic tails of DSPE-PEG-MAL with the GO surface followed by binding GRP to PEG (mGOCUG), CPT-11 was loaded by π–π interaction and SLP2 shRNA was complexed to obtain mGOCUG/CPT-11/shRNA (Fig. 1). We thoroughly analyzed the physico–chemical properties of nanocomposites during each preparation step as well as the drug release characteristics. Finally, the targeting efficacy and antitumor efficacy of test formulations were studied *in vitro* with U87 human glioblastoma cells and finally validated *in vivo* using an orthotopic U87 brain tumor xenograft model of nude mice.

2. Materials and methods

2.1. Preparation of mGO, mGOC, mGOCU and mGOCUG

Graphene nano-platelets were subject to modification following a modified Hummers' method.[52] Briefly, 1 g of graphene powder was stirred in 23 mL of sulfuric acid for 12 h, followed by addition of 3 g of $KMnO_4$ with continuous stirring for 30 min below 20 °C, 30 min stirring at 40 °C, and 45 min stirring at 80 °C. After adding 46 mL of distilled deionized water (ddH_2O), the solution was stirred at 98–105 °C for another 30 min, followed by cooling down to room temperature for 1 h. An additional 140 mL of ddH_2O and 10 mL of 30% H_2O_2 solution were added and reacted for 5 min at 40 °C. After the reaction, GO was washed three times with 5% HCl solution by centrifugation and dialyzed against ddH_2O until a neutral pH value was reached. Nano-sized GO was obtained by sonicating for 30 min and filtered with a 0.2 μm filter. Magnetic graphene oxide (mGO) was synthesized by chemical co-precipitation of Fe_3O_4 magnetic nanoparticles on the GO surface. We mixed 25 mg of GO, 108 mg of $FeCl_3{\cdot}6H_2O$ and 40 mg of $FeCl_2{\cdot}4H_2O$ (Fe^{3+} and Fe^{2+} ions in a 2 : 1 molar ratio) in 50 mL of ddH_2O and sonicated the solution for 30 min. The solution was

reacted under N_2 for 30 min and heated to 65 °C. Next, 1 g of chloroacetic acid was added to the solution and reacted for 1 h to convert the hydroxyl groups on GO into carboxylic acid groups, followed by the addition of 2 g of NaOH and reacted for additional 30 min. The GO was collected from the solution using a magnet and washed with copious ddH_2O.

Chitosan conjugated magnetic graphene oxide (mGOC) was synthesized by reacting 10 mg of mGO with 300 mg of chitosan (60 kDa molecular weight and 90% degree of acetylation) in 20 mL of 2-(*N*-morpholino)ethanesulfonic acid (MES) buffer (25 mM, pH 5) and sonicated for 30 min. Next, 40 mg of 1-ethyl-3-(3-dimethylaminopropyl) (EDC) were added to the mixture and incubated for 12 h at 4 °C for the formation of amide bonds between the carboxylate groups of mGO and the amine groups of chitosan. mGOC was recovered by magnetic separation and washed 2 times with ddH_2O. The amount of $-NH_2$ in mGOC estimated by the *o*-phthalaldehyde method was 3.15 ± 0.08 μmol mg^{-1} mGOC. To conjugate urocanic acid onto mGOC (mGOCU), a similar procedure was adopted as in mGOCU synthesis by reacting urocanic acid with mGOC, which formed amide bonds between –COOH groups of urocanic acid and $-NH_2$ groups of mGOC. Using a 1 : 2 molar ratio of $-COOH : -NH_2$, we reacted 2.6 mg of urocanic aid with 10 mg of mGOC in 20 mL of MES buffer (25 mM, pH 5) in the presence of 40 mg of EDC for 12 h at 4 °C. For the PEGylation of nanoparticles, 1 mg of mGOCU synthesized above was mixed with 0.35 mg of 1,2-distearoyl-*sn-glycero*-3-phosphoethanolamine-*N*-[maleimide(polyethylene glycol)-2000] (DSPE-PEG-MAL) in 1 mL of PBS and sonicated for 30 min at 5 W. The PEGylated mGOCU was separated from the solution with a magnet and washed with PBS.

To conjugate the gastrin releasing peptide (GRP), with the amino acid sequence Cys-Gly-Gly-Asn-Gln-Trp-Ala-Val-Gly-His-Leu-Met-NH_2, onto PEGylated mGOCU, maleimide groups of DSPE-PEG-MAL on the mGOCU surface were reacted with the thiol side group of N-terminal cysteine in GRP.[53] For this purpose, GRP (2 mg ml^{-1}, 0.75 ml) was mixed with the same volume of immobilised TCEP disulfide reducing gel for 1 h to break disulfide bonds formed between thiols of the cysteine side chains. After centrifugation at 1000*g* to remove the supernatant, the GRP was reacted with PEGylated mGOCU to form mGOCUG. The GRP concentration of the supernatant was quantified using the BCA protein assays kit (Bio-Rad) to calculate the amount of GRP conjugated to mGOCUG. Furthermore, to visualize the intracellular uptake of mGOCUG, 0.1 mg of mGOCUG was mixed with 1.875 μmol of 5(6)-carboxyfluorescein *N*-hydroxysuccinimide (NHS) ester for 1 h at room temperature, during which the NHS groups in fluorescein-NHS reacted spontaneously with the residual amine groups on the mGOCUG surface. After blocking the unreacted amine groups with glycine, the fluorescently labeled mGOCUG was recovered by magnetic separation and washed with ddH_2O as before.

2.2. Physico–chemical characterization

The particles size, polydispersity (PDI) and zeta potential of nanocomposites were analyzed by dynamic light scattering (DLS) using a Nano ZA90 Zetasizer (Malvern Instruments Ltd, Worcestershire, UK) at 25 °C. The particle suspension for DLS measurements was prepared by dispersing in ddH_2O at 0.1 mg mL^{-1}. The Fourier transform infrared (FTIR) spectra were recorded on a Horiba FT-730 FTIR spectrometer (Horiba Ltd, Tokyo, Japan) by blending samples with KBr powder, and scanned from 400 to 4000 cm^{-1} with 4 cm^{-1} resolution and at 2.5 mm s^{-1} scanning rate.

The morphology and size of nanoparticles were observed by transmission electron microscopy (TEM) (JEOL JEM-2000 EX II, Tokyo, Japan) at 100 kV. Before observation, the samples were diluted to 0.01 mg mL^{-1} in ddH_2O and then dropped on the surface of 200 mesh carbon-coated copper grid, followed by drying at 37 °C for 24 h. Thermogravimetric analysis (TGA) was conducted with 8 mg of dried powder samples under a nitrogen atmosphere from room temperature to 500 °C, with a heating rate of 10 °C min^{-1} using TGA2050 (TA Instruments, New Castle, DE). The X-ray diffraction (XRD) and Raman spectra were used to analyze the crystal structures of samples. For XRD analysis, a D2 Phaser X-ray powder diffractometer (Bruker, Madison, WI, USA) was used for scanning dried samples from 5° to 80° (2θ) with Cu Kα radiation. The step size was 0.02° (2θ value) per second. The crystalline size was determined using the Debye–Scherrer equation and the phase was compared with the JCPDS database for identification. The Raman analyses were recorded between 1100 and 2000 cm^{-1} with a Raman spectrometer with a laser excitation of 532 nm at 25 mW power. The magnetic characterization measurements were carried out with a superconducting quantum interference device (SQUID) magnetometer (MPMS XL-7, Quantum Design, San Diego, CA) at 25 °C and between −10 000 to 10 000 Gauss magnetic field. The weight percentage of Fe_3O_4 MNPs in different samples was determined by inductively coupled plasma optical emission spectrometry (ICP-OES, Varian 710-ES). The suspension stability was evaluated from the gross view of 1 mg mL^{-1} nanoparticles in PBS and in 10% fetal bovine serum (FBS) for up to 4 days and by measuring time-lapsed solution absorbance at 320 nm with an ultraviolet–visible (UV–Vis) spectrophotometer.

2.3. Drug loading and release

The loading of CPT-11 onto mGOCUG was achieved by mixing 0.2 mg of mGOCUG with various amounts of CPT-11 in 1 mL of PBS (pH 7.4) at 4 °C for 24 h, followed by magnetic separation. The supernatant was collected for the analysis of drug concentration by high performance liquid chromatography (HPLC) at 370 nm. An EclipseXDB-C18 column (250 mm × 4.6 mm) was used and 0.01 M pH 4 phosphate buffer/75% acetonitrile in a 40/60 volume ratio was the mobile phase flowing at 1 mL min^{-1} flow rate. The drug loading performance was calculated from the following equations.

$$\text{Loading efficiency}(\%) = \text{weight of CPT-11 loaded} / \text{weight of CPT-11 added} \times 100 \quad (1)$$

$$\text{Loading content}(\%) = \text{weight of CPT-11 loaded} / \text{weight of mGOCUG added} \times 100 \quad (2)$$

For drug release, mGOCUG/CPT-11 was prepared in 1 mL of PBS at pH 5.4 (endosomal pH) or at pH 7.4 (physiological pH). The solution was shaken at 150 rpm and 37 °C in the dark, followed by separating mGOCUG/CPT-11 with a magnet at predetermined time points. The supernatant was collected for the determination of drug concentration by HPLC as mentioned before. 1 mL of fresh PBS of the same pH value was added to replenish the volume of the removed supernatant and the drug release experiment was continued. The cumulative drug release (%) is calculated as,

$$\text{Cumulative drug release}(\%) = \sum \text{weight of CPT-11 released} / \text{weight of CPT-11 loaded} \times 100 \quad (3)$$

2.4. *In vitro* cell culture

2.4.1. Cell line and cell culture condition. The U87 human primary glioblastoma cell line was procured from American Type Culture Collection (ATCC HTB1, Manassas, VA, USA) and genetically modified by lentiviral infection for the steady expression of firefly luciferase to enable *in vivo* bioluminescence imaging. The cells were cultured in Dulbecco's Modified Eagle's Medium (DMEM) supplemented with 10% FBS and 1% penicillin/streptomycin at 37 °C in a humidified 5% CO_2 incubator.

2.4.2. Intracellular uptake. To investigate the intracellular uptake, U87 cells (1×10^4 cells) were seed on a 15 mm glass slide placed in each well of a 24-well cell culture plate and incubated for 24 h at 37 °C in a humidified CO_2 incubator containing 5% CO_2. Fluorescein-labeled mGOCUG or mGOCU (50 μg, green fluorescence) were separately added to each well and the plate was incubated for another 24 h. After removing the cell culture medium and washing with PBS three times, cells were fixed with 4% paraformaldehyde for 30 min. Next, the cell cytoskeleton was stained with 1 μg mL^{-1} phalloidin–tetramethylrhodamine B isothiocyanate (Phalloidin-TRITC, red fluorescence) for 30 min and the cell nucleus was visualized by counterstaining with 4,6-diamidino-2-phenylindole dihydrochloride (DAPI) (blue fluorescence) for 20 min. The intracellular uptake of nanoparticles was observed with a confocal laser scanning microscope (Zeiss LSM 510 Meta) at the excitation wavelength of 557/492/340 nm (red/green/blue) and emission wavelength of 576/517/488 nm (red/green/blue).

For the analysis of CPT-11 accumulation, the intracellular drug uptake efficiency was determined from the blue fluorescence intensity of CPT-11 by using flow cytometry analysis. U87 cells were seeded in the T-25 cell culture flasks at 5×10^5 cells per flask and incubated at 37 °C under 5% CO_2 atmosphere. After the incubation, cells were treated separately with free CPT-11, mGOCUG, mGOCU/CPT-11, or mGOCUG/CPT-11 at the same drug dosage (0.5 μg mL^{-1} CPT-11) for 2 h. Next, the cells were trypsinized and centrifuged at 2000*g* for 5 min to collect the cell pellet, followed by re-suspending the cell pellet in 500 μL of binding buffer. Analysis of fluorescence intensity corresponding to the intracellularly accumulated drug was performed using a FACS instrument (Attune NxT Flow cytometer, Life Technologies) with a 405 nm air-cooled argon laser as the excitation source. Fluorescence from cell-associated CPT-11 was detected using a 450 nm emission filter.

2.4.3. Endocytosis and endosomal escape. To investigate endocytosis and endosomal escape, U87 cells (1×10^4 cells) were seeded on a 15 mm glass slide placed in each well of a 24-well cell culture plate and incubated for 24 h at 37 °C in a humidified CO_2 incubator containing 5% CO_2. Fluorescein-labeled mGOCUG (50 μg) was added to each well and the plate was incubated for 2 and 24 h. After removing the cell culture medium and washing with PBS three times, cells were stained with 1 μM LysoTracker Red DND-99 (0.5 mL per well) for 1 h and the cell nucleus was visualized by counterstaining with DAPI for 20 min. The cells were observed under a confocal laser scanning microscope (Zeiss LSM 510 Meta) at the excitation wavelength of 577/492/340 nm (red/green/blue) and the emission wavelength of 590/517/488 nm (red/green/blue). As a control, fluorescein-labelled mGOCG was prepared similar to mGOCUG but without urocanic acid and endocytosis and endosomal escape were studied after incubation with U87 cells for 24 h.

2.4.4. Transfection of U87 Cells. To facilitate analysis of SLP2 gene expression with siRNA, we used a SLP2 shRNA plasmid DNA (SLP2-shRNA-PGLV3/GFP) co-expressing SLP2 shRNA and green fluorescent protein (GFP) in this study. The plasmid (64 kDa molecular weight) contains a pGLV3/H1/GFP/Puro vector and encodes the 19 nucleotide shRNA for knocking down the SLP2 gene expression.[54] After complexation of shRNA DNA plasmid with mGOCUG, the complex enters the cells through transfection and the cells can transcribe the foreign DNA to generate SLP2 shRNA. After the endoribonuclease Dicer processes the shRNA into siRNA by removing the loop sequence, the resulting siRNA can bind with a RNA-induced silencing complex (RISC) and separates the two strands of the RNA for activating the complex. The RISC remains bound to one strand, which complementarily binds to targeted SLP2 mRNA and cleaves it. This leads to SLP2 gene silencing and suppresses the production of the SLP2 protein. To investigate SLP2 shRNA transfection of U87 cells from expressed GFP fluorescence intensity, U87 cells were seeded in a 24-well cell culture plate at a seeding density of 5×10^3 cell per well and cultured for 24 h. The mGOCUG/SLP2-shRNA-PGLV3/GFP (mGOCUG/shRNA) complexes were prepared by mixing mGOCUG and SLP2 shRNA plasmid DNA for 30 min at room temperature, at weight ratios from 20 to 200 (w/w), followed by incubation for 3 days. After removing the medium and washing each well with PBS, the gene delivery efficiency was measured by observing the green fluorescence of expressed GFP under an inverted fluorescence microscope (Olympus

IX-71, Tokyo, Japan). The transfection efficiency was calculated from,

$$\text{Transfection efficiency}(\%) = \frac{\text{number of green fluorescent cells}}{\text{number of total cells}} \times 100 \quad (4)$$

2.4.5. Agarose gel electrophoresis assay and cell migration assay. The mGOCUG/SLP2-shRNA-PGLV3 complexes prepared with various weight ratios were run on 0.8% agarose gel in 0.5× TAE buffer at 100 V for 25 min and the electrophoretic mobility was investigated to evaluate the quantity of complexed shRNA plasmid DNA. Naked plasmids were used as controls.

The cell migration ability of transfected U87 cells, prepared with 1 : 80 (w/w) SLP2-shRNA-PGLV3/GFP : mGOCUG, was evaluated by the wound healing assay after removing non-transfected cells with 2 μg mL^{-1} puromycin. A Culture-Insert 2 Well in μ-Dish 35 mm culture inserts (ibidi GmbH) was placed in a cell culture dish. U87 cells treated with shRNA plasmid DNA for 3 days were seeded to the insert at a seeding density of 2×10^4 cells and cultured for 24 h to reach a confluent cell layer. Cells treated with mGOCUG alone were used as a control. After removing the center silicone strip, a cell-free gap was created within the cell layer, from which the cell migration could be observed as in wound healing assays. The cells were cultured in 2 mL of cell culture medium containing 5% FBS for different times and images were taken by optical microscopy to monitor time-dependent wound recovery. Using the ImageJ software, the recovery of wound area was calculated as,

$$\text{Wound area}(\%) = (\text{initial wound area} - \text{final wound area})/\text{initial wound area} \times 100 \quad (5)$$

2.4.6. *In vitro* cytotoxicity. To evaluate the cytotoxicity of the test sample, U87 cells were seeded in a 96-well cell culture plate at a seeding density of 5×10^3 cell per well and cultured overnight at 37 °C in a humidified 5% CO_2 incubator. After washing with PBS, the cells were incubated with 100 μL of CPT-11, mGOCU-CPT11, or mGOCUG-CPT11 solution prepared in culture medium, of different CPT-11 concentrations, to determine the IC50 (half-maximum inhibitory concentration) value. Cell viability after 48 h was obtained from the 3-(4,5-dimethylthiazol-2-yl)-2,5-diphenyl tetrazolium bromide (MTT) assay by reacting cells with 0.1 mL of MTT reagent for 2 h. After dissolving the crystal formed from the reduction of the MTT reagent by the mitochondria activity of live cells with dimethyl sulfoxide, the solution absorbance was determined using an enzyme-linked immunosorbent assay (ELISA) plate reader. The relative cell viability at different CPT-11 concentrations was calculated by normalizing the absorbance with those from cells culture with cell culture medium (taken as 100%). To evaluate the biocompatibility of drug-free nanocarrier, similar procedures were followed using U87 cells and 3T3 fibroblasts. After contacting cells with 0.001 to 100 μg mL^{-1} mGOCUG for 24, 48 and 72 h, we used the MTT assay to determine the relative cell viability as before.

2.4.7. Apoptotic measurement by flow cytometry analysis. Flow cytometry analysis was performed to investigate the apoptotic mechanism of U87 cells in the presence of the test sample. Briefly, 2×10^5 cells U87 cells were seeded in a T-25 flask and treated with free CPT-11, mGOCUG, mGOCU-CPT11 or mGOCUG-CPT11 (10 mg mL^{-1} CPT-11) for 24 h. After trypsinization, detached cells were labelled with FITC-Annexin V/Propidium iodide (PI) for live, early apoptotic, late apoptotic and necrotic cells. The samples were analyzed using a CytoFLEX flow cytometer (Beckman Coulter, Brea, CA, USA).

2.4.8. Western blot analysis. To investigate the molecular anticancer mechanism as well as the knockdown of SLP2 gene, cellular apoptosis-related marker proteins, caspase-3 and phosphorylated extracellular signal-regulated kinases (phospho-ERK, p-ERK), as well as SLP2 protein were assessed by Western immunoblot analysis. For this purpose, 2×10^6 U87 cells were cultured in a T75 flask for 24 h. Cells were treated with CPT11, mGOCUG, or mGOCUG/CPT-11/shRNA (10 μg mL^{-1} CPT-11 and 1 μg mL^{-1} SLP2 shRNA for 3 days at 37 °C. To extract total protein, harvested U87 cells were treated with 1×RIPA lysis buffer containing protease inhibitor cocktail (Thermo Fisher Scientific) for 30 min on ice. After centrifugation to remove cell debris, the supernatant was collected for the determination of protein concentration by a BCA protein assays kit. The protein was heat-denatured at 95 °C for 10 min and separated by sodium dodecyl sulfate polyacrylamide gel electrophoresis at 50 V for 30 min and 100 V for 60 min. The gels were transferred to a polyvinylidene fluoride membrane and blotted with anti-caspase 3, anti-phospho-ERK, anti-SLP2 antibody, or anti-β-actin antibody overnight at 4 °C. After probing with horseradish peroxidase-conjugated secondary antibodies and color development with Western Chemiluminescent HRP substrate, the formed complexes were detected using a MultiGel-21 gel imaging system for the densitometric analysis of protein bands by ImageJ software.

2.4.9. *In vitro* hemolysis study. To examine blood compatibility, possible hemolysis induced by test materials was analyzed *in vitro*. In brief, red blood cells (RBCs) from Sprague-Dawley (SD) rats were acquired by removing serum from the whole blood by centrifugation at 4 °C. The cells were diluted ten times with PBS and 0.3 mL of diluted suspension of RBCs was mixed with 1 mL of deionized water (positive control), 1 mL of PBS (negative control), or 1 mL of mGOCUG solution at different concentrations. The mixtures were incubated at 37 °C for 2 h and centrifuged at 4 °C for 5 min. The absorbance values of the supernatants were recorded using an UV–Vis spectrophotometer from 500 to 650 nm and compared at 540 nm (OD_{540}) for all the samples.

2.5. Animal study

2.5.1. Xenograft brain tumor mouse model. All animal experiments were performed in accordance with the Guidelines of the Declaration of Helsinki, and approved by the Institutional Animal Care and Use Committee at Chang Gung

University. BALB/c nude mice (4–5 weeks old, female) purchased from the National Laboratory Animal Center (Taipei, Taiwan). The U87 orthotopic xenograft tumor model was established by the intracranial administration of 3 μL of cell culture medium containing 3×10^5 U87 cells to the right intracranial region of each mouse to a 3 mm depth.

2.5.2. Brain tumor targeting. To confirm brain tumor targeting, mGOCUG/CPT-11 was labelled with Cyanine 5.5-NHS ester (Cy5.5-NHS), followed by mixing with shRNA at a weight ratio of 100. The resulting mGOCUG/CPT-11/shRNA formulation was intravenously injected into tumor-bearing mice with or without magnetic guidance. For magnetic guidance, a magnet was placed at the vicinity of the brain tumor site. The mouse in the control group was injected with normal saline. Four hours after administration, the mice were subject to near infrared fluorescence imaging with a non-invasive *in vivo* imaging system (IVIS) (Xenogen IVIS-200, Caliper Life Sciences). The mice were sacrificed and brain tissues harvested to determine the accumulation of Cy5.5-conjugated mGOCUG/CPT-11/shRNA in the brain tumor region using IVIS.

2.5.3. *In vivo* anti-tumor efficacy. Eight days after U87 cell implantation, the tumor-bearing mice were randomized into four groups (n = 8, each group), followed by intravenous injection of 200 μL of different sample on day 11 and 14. The study groups included the following: 1, normal saline (control); 2, mGOCUG; 3, CPT-11 + shRNA (7.5 mg kg^{-1} CPT-11 and 2.5 mg kg^{-1} shRNA); 4, mGOCUG/CPT-11/shRNA (7.5 mg kg^{-1} CPT-11 and 2.5 mg kg^{-1} shRNA) with magnetic guidance by placing a magnet at the vicinity of the tumor site for 30 min. At the day of tumor size analysis, each mouse was anesthetized with 1% isoflurane followed by intraperitoneal injection of 200 μl of D-luciferin solution at a dose of 150 mg luciferin per kg body weight. Bioluminescence imaging (BLI) was conducted using IVIS (Xenogen IVIS-200, Caliper Life Sciences) to determine the peak bioluminescence. The BLI intensity was acquired from the total bioluminescence signal intensity in the tumor and BLI intensity standardization was carried out by dividing the BLI signal intensity at a specific time with that on day 8 when randomizing the mice, which is $\sim 1 \times 10^7$ p s^{-1}. The body weight of mouse was recorded daily and animals were sacrificed when they lost more than 20% of initial body weight or showing hemiparesis, back hunk and seizures, from which the survival time of tumor-bearing mice was determined.

2.5.4. Histological, immunohistochemical and hematologic analyses. For histology, tumors were harvested after euthanizing the mice on day 18 post-implantation, and tumor tissues were immediately fixed in 10% phosphate buffered formalin, followed by paraffin-embedment and sectioning to 3–5 μm thickness for hematoxylin and eosin (H&E) staining. As for immunohistochemical (IHC) staining, another set of tissue slices were incubated with rabbit primary antibody against Ki-67, p-ERK, or SLP2 at 4 °C for 24 h to detect the protein expression. After incubating with HRP-conjugated anti-rabbit secondary antibody (ImmPRESS® HRP universal antibody, anti-rabbit IgG produced in horse) for color development, counterstained with hematoxylin for nucleus, images were taken under an inverted microscope. The PAX-it image analysis software was used to quantify the protein expression level from IHC staining in each picture frame's region of interest (ROI), using the area percentage of the immune-reactive area within the ROI. To evaluate systemic toxicity, blood samples were collected for hematological analysis (red blood cell count, white blood cell count, platelet count, hemoglobin and hematocrit). The mice in the control group were used for comparison.

2.6. Statistical analysis

All results are reported as the mean ± standard deviation (SD). To compare means of different groups, one-way analysis of variance (ANOVA) analysis was performed using the SPSS software. Differences were considered to be significant at $p < 0.05$.

3. Results and discussion

3.1. Characterization of magnetic nanocomposites

The nanocomposites prepared during each synthesis step in Fig. 1 were characterized by different techniques. The morphology was observed under TEM (Fig. 2A), which shows the laminar stacking form of GO and magnetite in mGO after the chemical co-precipitation of Fe_3O_4 on GO. By sequential modification with chitosan (mGOC), urocanic acid (mGOCU), and GRP (mGOCUG), the surface roughness apparently increased, but with no significant change of surface morphology. The particles are platelet shaped from the shape of GO. Nonetheless, the drug-loaded mGOCUG/CPT-11/shRNA showed a larger particle size from TEM, which is supported from the dynamic light scattering (DLS) analysis of the distribution of the average particle size (Fig. 2B). As shown in Table 1, the average hydrodynamic diameter consistently increased during the sequential modification/conjugation steps from GO (122 nm) to mGOCUG/CPT-11/shRNA (355 nm), owing to increasing amount of molecules being grafted to GO. In a desirable drug delivery system, the optimal polydispersity index (PDI) is expected to be below 0.3, for uniform particle size distribution as well as good suspension stability.[55] The mean PDI values of all GO-based composites were below 0.3 (Table 1).

From electrophoretic mobility measurements, GO showed a highly negative zeta potential value (−40.8 mV) with abundant oxygen-containing functional groups on its surface (Fig. 2C). The surface potential slightly changed to −35.8 mV for mGO due to the residual ammonium ions associated with Fe_3O_4 since ammonia was used during the chemical co-precipitation step. The zeta potential value changed dramatically and became positive (38.7 mV) for mGOC, owing to the consumption of carboxylate groups on GO after amide bond formation as well as the remnant protonated primary amine groups in the chitosan backbone. The zeta potential shifted to 29.8 mV for mGOCU by carefully controlling the amount of urocanic acid used for reaction. By setting the molar ratio between

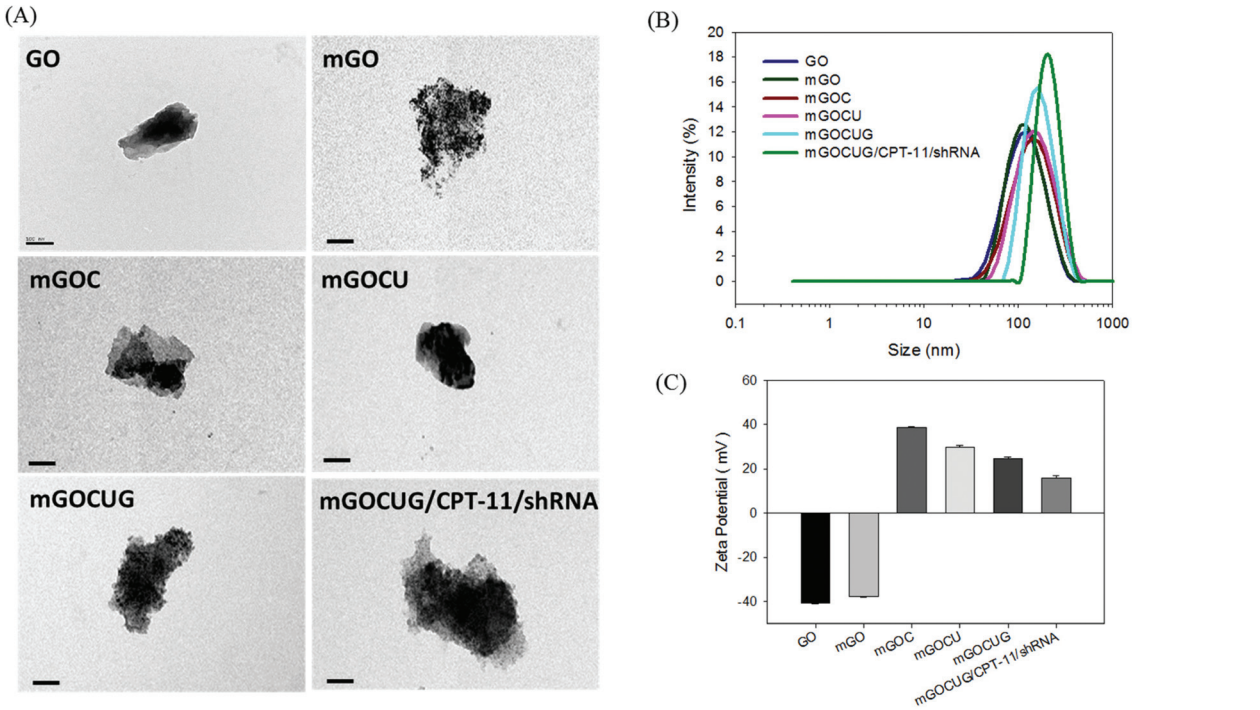

Fig. 2 Characterization of nanocomposites by transmission electron microscopy (TEM) (bar = 100 nm) (A), dynamic light scattering (DLS) (B), and zeta potential (C).

Table 1 The average particle size and polydispersity from dynamic light scattering analysis (mean ± SD, n = 3)

Sample	Average particle size (nm)	Polydispersity (PDI)
GO	122 ± 8	0.28 ± 0.03
mGO	129 ± 6	0.29 ± 0.07
mGOC	185 ± 10	0.25 ± 0.10
mGOCU	199 ± 11	0.21 ± 0.05
mGOCUG	237 ± 13	0.28 ± 0.07
mGOCUG/CPT-11/shRNA	355 ± 17	0.27 ± 0.08

$-NH_2$ in chitosan and –COOH in urocanic acid at 2 : 1 during the reaction, we intend to obtain mGOCU with abundant positively charged amine groups for complexation with shRNA plasmid DNA. The zeta potential shifted to 24.8 mV for mGOCUG after modification with negatively charged molecules DSPE-PEG-MAL and GPR.[53] As expected, the positive zeta potential further dropped to 15.9 mV for mGOCUG/CPT-11/shRNA after binding with the highly negative shRNA plasmid DNA, albeit still with a value high enough for colloidal stability (Fig. 2C).

Raman spectroscopy is often applied to characterize GO and its derivatives by investigating the disorder and defects in the crystal structure. The Raman spectra of GO and mGO are shown in Fig. 3A. GO displays two strong peaks at 1339 and 1597 cm^{-1}, corresponding to the D and G-bands, respectively. The corresponding values in mGO shifted little and were at 1340 and 1591 cm^{-1} as expected. The G band is attributed to the first order scattering of the sp^2 carbon–carbon bond,[56] while the D-band represents the defect sites associated with vacancies and grain boundaries.[57] Most importantly, the I_D/I_G value of mGO (0.84) was identical to that of GO, confirming that no significant change in the crystal structure occurred after co-precipitation of Fe_3O_4 MNPs on the GO surface. The X-ray diffraction (XRD) patterns of GO, Fe_3O_4 MNPs, and mGO are illustrated in Fig. 3B. GO demonstrated a typical diffraction peak at 2θ = 11.4°, which could be indexed to the (002) plane of a cubic cell. For mGO, new peaks corresponding to the (220), (311), (400), (422), (511) and (440) planes of Fe_3O_4 MNPs (JCPDS no. 19–0629) are formed at 2θ = 30.3°, 35.7°, 43.2°, 53.4°, 57.4° and 63.0°, respectively, indicating the presence of pure magnetite in mGO.[58] In addition, the crystallite sizes of magnetite, obtained by using the Debye–Scherrer equation from the strongest (311) reflection peak, were 11.5 nm and 14.2 nm for Fe_3O_4 and mGO, respectively, to support the formation of nano-sized MNPs in mGO by chemical co-precipitation.

The thermal properties of moieties conjugated to GO as well as synthesized nanocomposites were investigated by thermogravimetric analysis (TGA), Fig. 3C. GO was thermally unstable and showed substantial weight loss from 130 to 250 °C, due to the decomposition of its labile oxygen-containing functional groups, with a peak decomposition temperature at 200 °C and 36.5% residual weight at 600 °C.[59,60] Fe_3O_4 MNPs underwent minimal weight loss (~4%) from the loss of –OH functional groups on its surface.[61] For mGO, after the

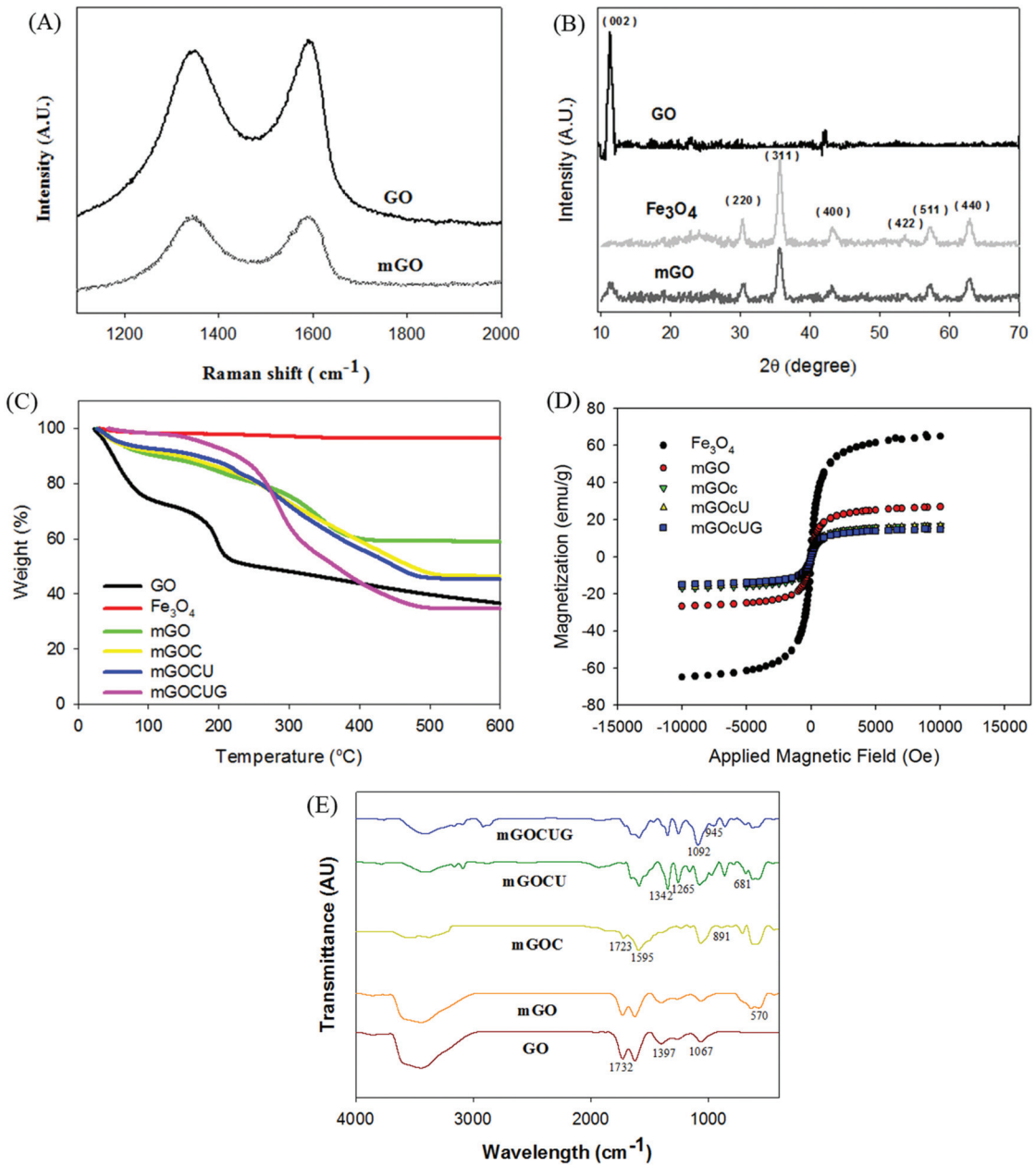

Fig. 3 Characterization of nanocomposites by Raman spectroscopy (A), X-ray diffraction (XRD) (B), thermogravimetric analysis (TGA) (C), superconducting quantum interference device (SQUID) (D) and Fourier transform infrared (FTIR) spectroscopy (E).

chemical co-precipitation of MNPs, thermal decomposition was delayed until 300–400 °C and the residual weight increased to 59.0% due to the thermal stability of Fe_3O_4. The TGA curves for mGOC, mGOCU and mGOCUG revealed additional weight loss at a temperature corresponding to chitosan, urocanic acid and DSPE-PEG-MAL, suggesting the successful modification/conjugation of mGO with these molecules. The final residual weight was also in the order of mGOC (46.3%) > mGOCU (45.2%) > mGOCUG (34.6%), as each grafting step introduced additional thermally degradable molecules and contributed to additional weight loss at 600 °C. These values may be compared with the GRP content in mGOCUG from BCA protein analysis, where 0.135 mg of GRP per mg of mGOCUG was obtained.

Fig. 3D reveals the hysteresis curves of the nanocomposites from the superconducting quantum interference device (SQUID) analysis at room temperature. The saturation magnetization values were 64.9, 26.7, 16.8, 16.5 and 14.8 emu g^{-1} for Fe_3O_4, mGO, mGOC, mGOCU, and mGOCUG, respectively. The saturation magnetization of mGO reduced to 41.1% of that of Fe_3O_4, consistent with its content from ICP-OES analysis (42.4 ± 1.6%) in mGO. A reduced weight percentage of

MNPs in a sample for SQUID analysis may lead to a diminished saturation magnetization value.[62] Therefore, further grafting with chitosan, urocanic acid, DSPE-PEG-MAL and GRP on mGO decreased the weight percentage of magnetizable MNPs in the nanocomposite, and reduced the saturation magnetization value to 25.9%, 25.4% and 22.8% of that of Fe_3O_4 for mGOC, mGOCU and mGOCUG, respectively. These values are supported from the Fe_3O_4 contents from ICP-OES, which are 25.8 ± 0.4%, 25.8 ± 0.6% and 21.0 ± 0.3%. From the magnetization curve, the remnant magnetization value were all close to zero and no hysteresis loop was observed, suggesting Fe_3O_4 MNPs retained the characteristic superparamagnetic behavior during the synthesis of mGOCUG. The superparamagnetic property is crucial for *in vivo* application as the drug-loaded magnetic nanocomposites should be easily dispersed at the targeted site after removing the external magnetic field. This will avoid undesirable agglomeration and possible vessel blockage.[63]

From FTIR spectroscopy analysis, the GO spectrum shows characteristic peaks at 1067, 1397 and 1732 cm^{-1} respectively, corresponding to C–O–C stretching, C═C stretching and C═O stretching of the carboxyl group. In the spectrum of mGO, a new characteristic peak appears at 570 cm^{-1} due to the stretching vibration of the Fe–O bond in Fe_3O_4. For mGOC, the bands at 1723 and 1595 cm^{-1} could be assigned to the amide I (C═O) and amide II (N–H) bonds, respectively. A new band appears at 891 cm^{-1} as well from the glucosidic C–O–C stretching in chitosan. The urocanic acid in mGOCU contributes to a new band at 681 cm^{-1} from the combination of ν(C–N) and δ ring modes of imidazole. A new band at 1265 cm^{-1} appears as well from the combination of δ(C–C) and δ(C–N) modes of the imidazole ring while the 1342 cm^{-1} peak can be assigned to the ring stretch. For mGOCUG, a new peak at 945 cm^{-1} arises due to the P–O–C bonding in DSPE-PEG-MAL. The imidazole groups in histidine residues of GRP also increase the 1092 cm^{-1} peak intensity after conjugation of the peptide ligand.

As the drug/gene carrier is designed for *in vivo* cancer treatment, it is imperative to determine their suspension stability. The suspension stability of mGOCUG/CPT-11/shRNA was examined in pH 7.4 PBS buffer (Fig. 4A) and in 10% fetal bovine serum (FBS) (Fig. 4B). The results revealed that mGOCUG/CPT-11/shRNA can form a well-dispersed solution without visible precipitation and significant change of solution absorbance under physiologically relevant conditions for up to 4 days, endorsing its suitability for intravenous administration.

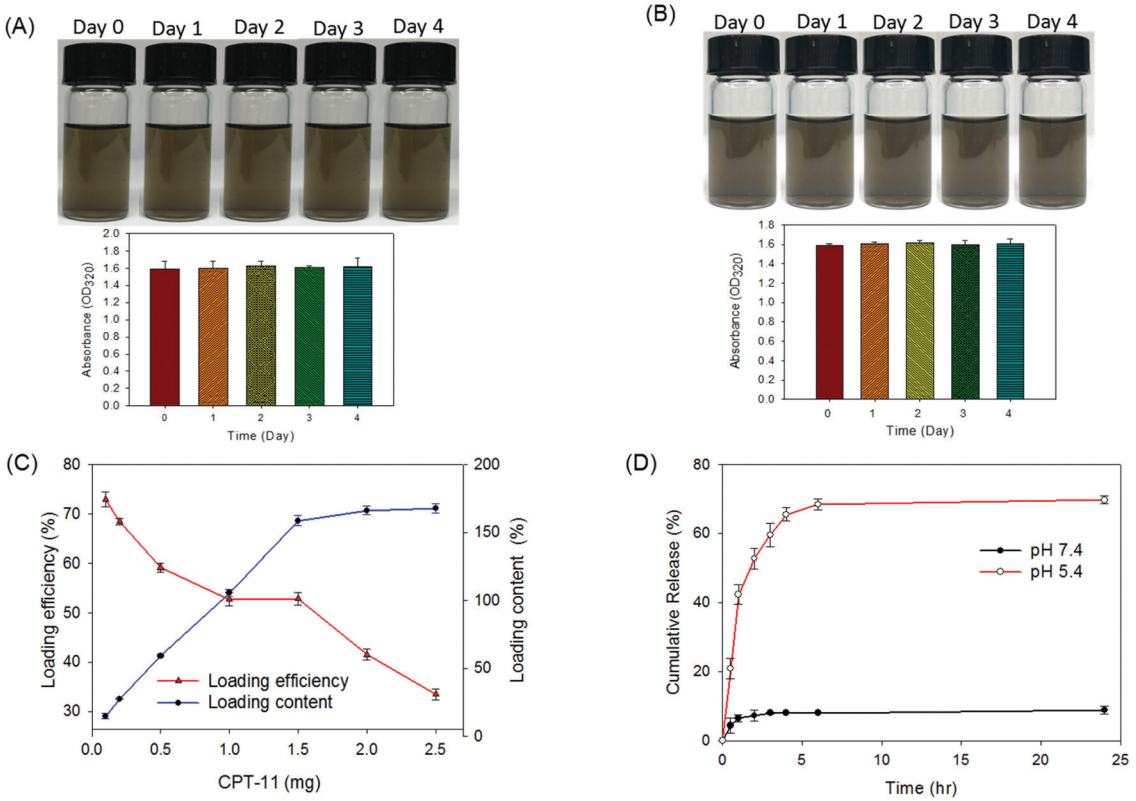

Fig. 4 The suspension stability of mGOCUG/CPT-11/shRNA from gross view and by quantifying solution absorbance at 320 nm (OD_{320}) in pH 7.4 PBS (A) and 10% fetal bovine serum (FBS) (B). The drug loading efficiency and drug loading content when a CPT-11 solution with different initial concentration was reacted with 0.5 mg mGOCUG (C). The cumulative drug release profiles of CPT-11 from mGOCUG/CPT-11 in PBS (pH 5.4 or pH 7.4) at 37 °C (D).

3.2. Drug loading and release

Considering that drug loading and release behavior are the most crucial characteristics to evaluate a drug delivery system, an optimal formulation for loading CPT-11 on mGOCUG was investigated. The loading efficiency and loading content of CPT-11 on mGOCUG are illustrated in Fig. 4C, when 0.5 mg of mGOCUG was mixed with increasing amount of CPT-11. By increasing the amount of CPT-11 from 0.1 to 2.5 mg, the drug loading content (weight of CPT-11 loaded per unit weight of mGOCUG) increased from 14.6% to 167.4%. In contrast, the loading efficiency (weight percentage of initial CPT-11 loaded on mGOCUG) decreased from 72.9% to 33.5%. It was evident that a dramatic increase in the drug loading content resulted in a detrimental decrease in loading efficiency. Since the space available for CPT-11 binding by π–π stacking on the mGOCUG surface is limited, the loading content demonstrates saturation by approaching the maximum value when the concentration of CPT-11 reaches 1.5 mg, which coincides with a rapid decrease of the drug loading efficiency thereafter. To acquire an optimal formulation, an ideal tradeoff between the loading content and loading efficiency should be taken into account. Thus, we chose the formulation by reacting 1.5 mg of CPT-11 with 0.5 mg of mGOCUG as the best formulation in the following studies, which is with 158.5% drug loading content and 52.8% drug loading efficiency.

Since it is desirable that a drug nanocarrier can release loaded drug after endocytosis for maximal therapeutic efficacy, a pH-sensitive drug release behavior of mGOCUG/CPT-11 is desirable and should be confirmed. Thus, the release of CPT-11 from mGOCUG/CPT-11 was investigated from the cumulative percentage of released CPT-11 at 37 °C in PBS at pH 5.4 and pH 7.4, to simulate the endosomal environment and the physiological condition, respectively. As shown in Fig. 4D, nearly ten times more CPT-11 was released at pH 5.4 (62.3%) than at pH 7.4 (6.4%) within 1 h, confirming the burst release of the drug in an acidic environment of endosomes. Furthermore, the sustained release of CPT-11 from mGOCUG/CPT-11 was noted at longer times, where the percentage of released CPT-11 at pH 5.4 (71.7%) is still maintained at a high value (8.2 folds) compared with that at pH 7.4 (8.8%) in 24 h, supporting the pH-responsive CPT-11 release. The adsorption of CPT-11 to mGOCUG involves hydrogen bonding between the hydroxyl groups in CPT-11 and the carboxyl groups in mGOCUG. As hydrogen bond formation is pH-dependent, more protons will compete with the functional groups responsible for hydrogen bonding at pH 5.4 than at pH 7.4. This will weaken the interactions between CPT-11 and mGOCUG, which ultimately promote the release of CPT-11 at pH 5.4. Taken together, the cytotoxicity of mGOCUG/CPT-11 toward cancer cells is expected to improve from free CPT-11 by releasing the drug cargo in an acidic endosomal environment after intracellular uptake.

3.3. Intracellular uptake and flow cytometry analysis

The high expression of GRPR on the U87 cell surface is anticipated to facilitate the active targeting of U87 cells by using GRP as a ligand. This targeting effect can contribute to a significant accumulation of the loaded drug and further enhance the therapeutic efficiency in comparison with the administration of free drug.[64,65] The intracellular uptake efficiency of fluorescein-labeled mGO was investigated under a confocal microscope, after staining the cell cytoskeleton with red fluorescence-producing Phalloidin-TRITC and the nucleus with blue fluorescence-producing DAPI (Fig. 5A). After incubating nanocomposites with U87 cells for 24 h, the confocal images revealed that U87 cells demonstrated a significantly higher uptake rate of mGOCUG than mGOCU, where the green fluorescent signal from mGOCUG was shown to be exclusively localized within the red fluorescent cytoskeleton, yielding the yellow fluorescent spots in the merged images. Enhanced internalization of mGOCUG by U87 cells could therefore be achieved through active targeting with GRP-conjugated nanocomposites.

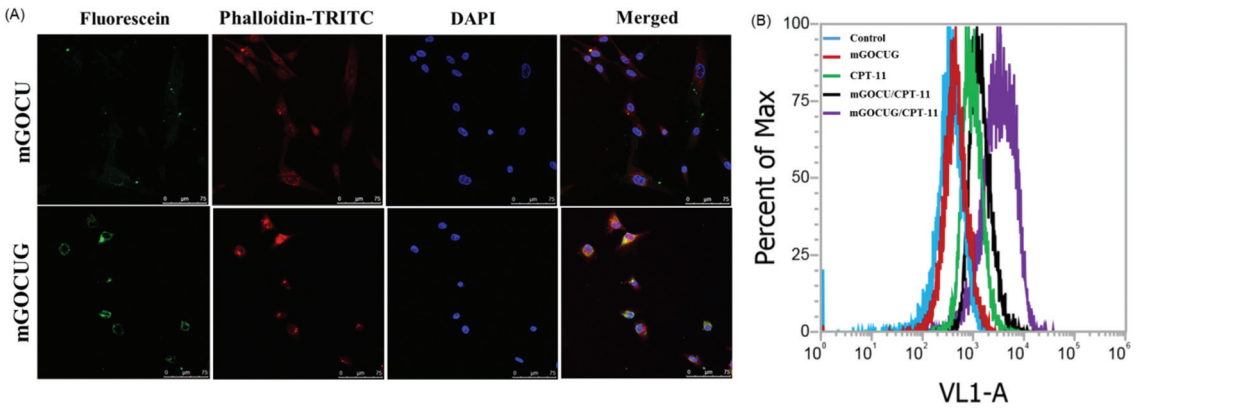

Fig. 5 (A) Intracellular uptake of fluorescein-labelled mGOCU and mGOCUG (green) after incubating with U87 cancer cells for 24 h. The cell cytoskeleton and nucleus were stained separately with Phalloidin-TRITC (red) and DAPI (blue) and observed by confocal laser scanning microscopy (Bar = 75 μm). (B) The intracellular drug uptake from flow cytometry analysis of CPT-11 blue fluorescence after incubating U87 cells with different samples for 24 h.

As cytotoxicity toward cancer cells is correlated with the intracellular drug concentration, the effectiveness of mGOCUG over mGOCU as a CPT-11 nanocarrier was further investigated from flow cytometry analysis of the intracellular drug concentration, by taking advantage of the blue fluorescence signal associated with CPT-11. Consistent with the trend observed from confocal microscopy (Fig. 5A), the highest intracellular CPT-11 concentration was found for mGOCUG/CPT-11 through ligand-mediated cellular trafficking (Fig. 5B). The geometric mean intensities are 403, 514, 1061, 1568 and 5169 for control, mGOCUG, CPT-11, mGOCU/CPT-11, and mGOCUG/CPT-11, respectively. By exhibiting 3.3-fold higher uptake rate of CPT-11, the results further underline the importance of GRP-mediated targeted drug delivery, which can augment cytotoxicity toward GRPR-overexpressing U87 cells.

As the metabolic enzyme lysosome can degrade internalized nanoparticles along with their complexed gene drugs, a plasmid DNA-loaded nanocomposite should escape from the lysosomes once internalized, to avoid being degraded resulting in efficient systemic siRNA delivery.[39] As shown in Fig. 6, the lower localization of fluorescein-labelled mGOCUG (green) within lysosomes, at 24 h compared to that at 2 h, indicates possible endosomal/lysosomal escape. Furthermore, by comparing with the uptake of fluorescein-labelled mGOCG at 24 h, which was prepared similar to mGOCUG but without urocanic acid conjugation, most mGOCG nanoparticles were still trapped within the endosomes/lysosomes with yellow fluorescence signal around the cell nucleus from merged green and red fluorescence. This is consistent with the finding that imidazole ring in urocanic acid plays an important role in endosomal/lysosomal escape through proton sponge mechanism, and therefore enhance the release of the complex into the cytoplasm following endocytosis.[66] Taken together, the confocal microscopy analysis confirms the intercellular uptake of mGOCUG by U87 cells *via* an endocytosis internalization pathway followed by endosomal escape to facilitate shRNA delivery.

3.4. Gene delivery, gene silencing and migration inhibition of U87 cells with SLP2 shRNA

A non-viral vehicle for the delivery of shRNA is commonly a cationic preparation with its positive charge facilitating complexation with negatively charged nucleic acids. Hence, after chitosan modification, the cationic mGOCUG nanocarrier was chosen as the vehicle for the condensation and protection of SLP2 shRNA plasmid DNA. The optimum mGOCUG/nucleic acid payload ratio was evaluated by agarose gel electrophoresis, as the formed complexes will be retained in wells and only free nucleic acid can migrate to the positive electrode on gels. Furthermore, as chitosan was modified by urocanic acid in mGOCUG, the amount of urocanic acid grafted to chitosan, which consumes primary amine groups and influences binding affinity, also needs study. Therefore, we tested two formulations by conjugation mGOC with urocanic acid at a –COOH/–NH_2 (C/N) molar ratio of 0.5 and 0.25. As shown in Fig. 7A, the mGOCUG/shRNA complex showed a gradual rise in the retarded proportion of shRNA as the mGOCUG/shRNA (G/R) mass ratio increased, especially at G/R ratios higher than 40. This trend could be assigned to the change of the surface charge of the complexes where a positively charged complex will tend to be retarded. The zeta potential of mGOCUG/shRNA complexes prepared with different G/R ratios was thus examined. As shown in Fig. 7B, the zeta potential in both groups changed from a negative value to a positive one as the

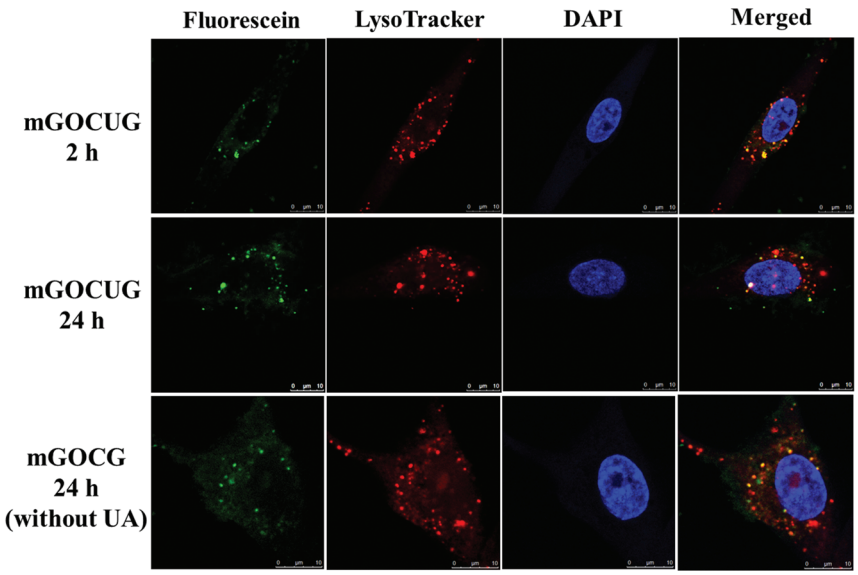

Fig. 6 Intracellular uptake of fluorescein-labelled mGOCUG after incubation with U87 cells for 2 h and 24 h. The intracellular uptake of fluorescein-labelled mGOCG in 24 h, which was prepared without using urocanic acid (UA) ad used as control group for comparison. The cell endosomes/lysosomes and nucleus were stained separately with LysoTracker (red) and DAPI (blue), and observed by confocal laser scanning microscopy. Bar = 10 μm.

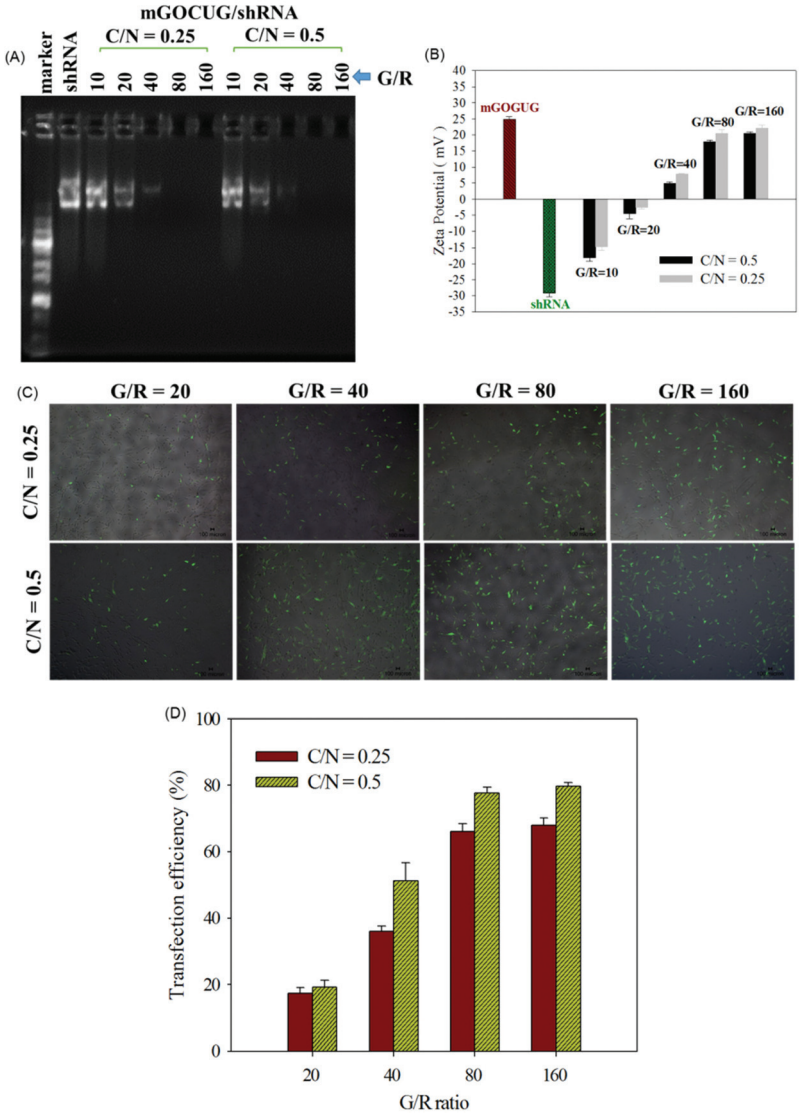

Fig. 7 The characterization of mGOCUG/shRNA prepared with different –COOH/–NH_2 (C/N) molar ratios during the preparation of mGOCUG with urocanic acid/chitosan, and different mGOCUG/shRNA (G/R) mass ratios for shRNA complexation by agarose gel electrophoresis assays (A) and zeta potentials (B). The fluorescence microscopic images of U87 cells after transfection with mGOCUG/shRNA (bar = 100 μm) (C), and the transfection efficiency determined from the ratio of U87 cells expressing green fluorescent protein (GFP) (D).

G/R ratio exceeds 40 and reaches a plateau value at ~25 mV when the G/R ratio is beyond 80. A lower C/N value, where less –NH_2 in chitosan is used for conjugation with urocanic acid, a complex with a higher positive charge was obtained. This trend is consistent with the gel electrophoresis results in Fig. 7A.

Using the trend observed from the surface change of the complexes, we next studied the influence of C/N and G/R ratios on the transfection efficiency of mGOCUG/shRNA, to ensure that the shRNA plasmid DNA could exert its RNAi effect on U87. This was first observed from the expression of green fluorescent protein (GFP) that is encoded in SLP2 shRNA plasmid DNA. The U87 cells transfected with mGOCUG/shRNA for 3 days were examined under fluorescence microscope, which showed different GFP-expressing cell population for mGOCUG prepared with different C/N or G/R ratios (Fig. 7C). For the quantitative evaluation of the transfection efficiency, the percentage of transfected U87 cells was calculated and is shown in Fig. 7D. The mGOCUG/shRNA complexes exhibited an increasing trend of transfection efficiency as the G/R ratio increased, reaching a plateau value at 80, which were 63% and 79% for C/N of 0.25 and 0.5, respectively. That a higher C/N value leads to higher transfection underlines the importance of urocanic acid for endosomal escape over nucleic acid payload loading. Taken together, mGOCUG/shRNA prepared with G/R = 80 and C/N = 0.5 was chosen as the preferred formulation owing to sufficient shRNA retain ability, overall cationic charge and the best transfection efficiency. Furthermore, mGOCUG/shRNA can also respond to an external magnetic

field due to the presence of magnetite. This characteristic is effective in guiding the nanocomposite to the targeted tissue in gene delivery as well as minimizing undesirable side effects. This ideal preparation was used in the following studies.

To confirm the successful silencing of the SLP2 gene, the western blot analysis of SLP2 protein synthesis in U87 cells, after transfection with different formulations, was conducted and the results are shown in Fig. 8A. There was no significant difference in the relative SLP2 protein expression in the control (medium) and the mGOCUG groups, while the shRNA group showed a moderate but significant reduction of SLP2 synthesis as expected (Fig. 8B). The SLP2 protein expression level was significantly reduced for the mGOCU/shRNA group from the shRNA group, announcing the preferred use of mGOCU as a nanocarrier for shRNA delivery in gene silencing over free shRNA. Most importantly, by using GRP for targeted gene delivery, the SLP2 protein expression level of the mGOCUG/shRNA group reduced to 60.4% that in the control group and significantly lower than all other groups, due to the enhanced internalization of the nanocomposite by U87 cells *via* endocytosis. We successfully demonstrated more effective SLP2 gene silencing through mGOCUG-mediated delivery of shRNA over free shRNA, which could be further enhanced significantly through targeted delivery with mGOCUG using GRP as a ligand.

Next, the wound-healing assay, which is an integrated process of cell proliferation and migration, was conducted to confirm the role of SLP2 gene silencing in the migration ability of U87 cells. As shown in Fig. 8C, the migration of U87 cells was repressed after silencing the SLP2 gene. In contrast, the cells in the control (medium) group migrated rapidly to the denuded area of the wound, leading to a higher wound closure rate within 12 h. The recovered wound area compared with the initial wound area in the SLP2 knockdown group was significantly less than those for the control group at 4 and 12 h (Fig. 8D). Overall, the results support that by knocking down the SLP2 gene, the proliferation and migration of U87 tumor cells will be inhibited, which may serve as a potential target in gene therapy for invasive U87 tumors *in vivo*.

3.5. *In vitro* biocompatibility

After confirming the cellular internalization characteristic, the biocompatibility of mGOCUG was carried out by exposing 3T3 (normal) cells and U87 (tumor) cells to various concentrations of mGOCUG for 24, 48 and 72 h. The cell viability was determined from MTT assays and normalized with that of control using medium alone for cell culture. As shown in Fig. 9A and B, the relative cell viability remained above 95% after contacting both cell lines with mGOCUG at concentrations up to 100 μg mL^{-1} in cell culture medium for 72 h, indicating that the cell viability was not affected by the internalization of the nanocarrier and that the prepared mGOCUG is biocompatible at concentrations suitable for *in vivo* injection. Besides cytocompatibility, further biocompatibility testing is through hemocompatibility to investigate whether nanoparticles may induce hemolytic response when delivered by intravenous injection. To conduct *in vitro* hemolysis assay, various concentrations of mGOCUG were mixed with rat red blood cell (RBC) samples at 37 °C for 1 h. Water and PBS were used as positive and negative hemolysis controls, respectively. The absorption spectra (Fig. 9C) of the supernatant of test solutions demonstrated that diluted RBC samples incubated with 100 to 800 μg

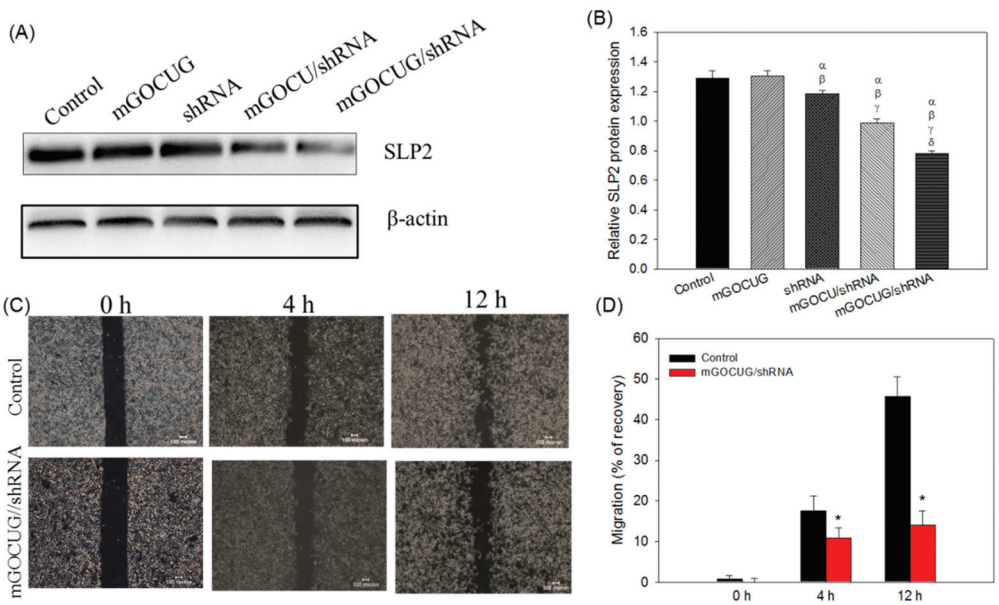

Fig. 8 (A) The SLP2 protein synthesis from western blot analysis and (B) the relative SLP2 protein expression using β-actin as a loading control after U87 cells were transfected with different formulations. $^{\alpha}p < 0.05$ compared with control; $^{\beta}p < 0.05$ compared with mGOCUG, $^{\gamma}p < 0.05$ compared with shRNA, $^{\delta}p < 0.05$ compared with mGOCU/shRNA. (C) The wound healing assays for cell migration ability (bar = 100 μm) and (D) the quantitative analysis of the recovered wound area compared with the initial wound area after U87 cells were transfected with mGOCUG/shRNA. $^{*}p < 0.05$.

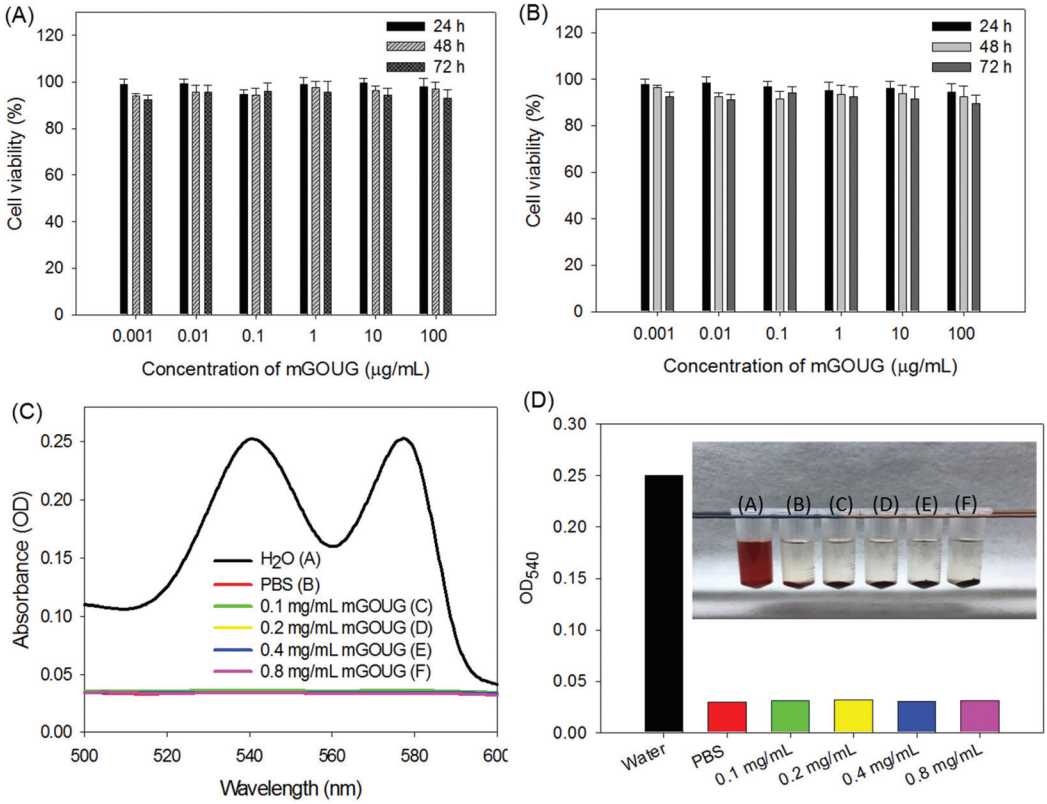

Fig. 9 The cytocompatibility of mGOCUG at different concentrations was determined by relative cell viability (relative to culture medium) using MTT assays after coming in contact with 3T3 fibroblasts (A) and U87 cells (B) for 24 h, 48 h and 72 h. The *in vitro* hemolysis test with diluted red blood cells was determined from the absorption spectra of the supernatant after incubation for 1 h for hemolytic assay (C). The optical density at 540 nm (OD_{540}) of the supernatant was shown in (D) with the insert demonstrating the gross view of samples.

mL^{-1} of mGOCUG (prepared in PBS) displayed undetectable optical density (OD) from 500 to 600 nm, which is similar to PBS. In contrast, the positive control group showed strong absorption peaks at 540 nm and 577 nm, corresponding to the rupture of RBCs in water and the release of oxyhemoglobin. The gross views of all samples (Fig. 9D) reveal no visible hemolysis and significant change of OD_{540} between all samples except water. Taken together, the outstanding cytocompatibility and hemocompatibility of mGOCUG underlines its excellent biocompatibility for *in vivo* application.

3.6. Cell cytotoxicity and apoptosis

Once substantiating the cellular internalization characteristic and the safety of the nanocomposites, cytotoxicity toward cancer cells was carried out to compare the chemotherapeutic efficacy of various treatments *in vitro*. For this purpose, free CPT-11, mGOCU/CPT-11 and mGOCUG/CPT-11 at different concentrations were incubated with U87 cells at 37 °C for 48 h. As shown in Fig. 10A, mGOCUG/CPT-11 exerted the most pronounced cytotoxic effect with the lowest IC_{50} (5.8 μg mL^{-1}), compared with that of mGOCU/CPT-11 (9.7 μg mL^{-1}), as well as with CPT-11 (14.6 μg mL^{-1}). Undoubtedly, the higher cytotoxicity shown by mGOCU/CPT-11 over free CPT-11 is due to nanocarrier-mediated drug delivery, where higher intracellular CPT-11 concentration was found when U87 cells were incubated with mGOCU/CPT-11 (Fig. 5B). The use of mGOCUG for CPT-11 delivery further enhances cytotoxicity toward U87, due to GPR-mediated drug delivery, with a higher intracellular uptake rate of mGOCUG and intracellular CPT-11 concentration (Fig. 5).

To further study the cytotoxicity mechanism, flow cytometry analysis was conducted by staining the cells with Annexin V/Propidium iodide (PI) and quantifying the percentage of live (Q_3), early apoptotic (Q_4), late apoptotic (Q_2) and necrotic (Q_1) cells, with differences in cell membrane permeability and integrity (Fig. 10B). The flow cytometry data showed that early and late apoptosis accounted for the major death mechanism when U87 cells are treated with CPT-11. Consistent with the cell viability results using MTT assay, mGOCUG demonstrated high biocompatibility with U87 cells, with comparable apoptosis rate (2.7%) with control (2.3%). The ratio of apoptosis cells treated with free CPT-11 was 7.0% and increased to 13.2% for mGOCU/CPT-11, to be consistent with a higher IC_{50} as shown in Fig. 10A. Additionally, the apoptotic ratio dramatically increased to 34.0% when treated with mGOCUG/CPT-11, endorsing the targeting effect of GRP. Undoubtedly, the GRP-mediated active targeting of mGOCUG/CPT-11 could enhance its endocytosis by U87 cells considerably and increase the cyto-

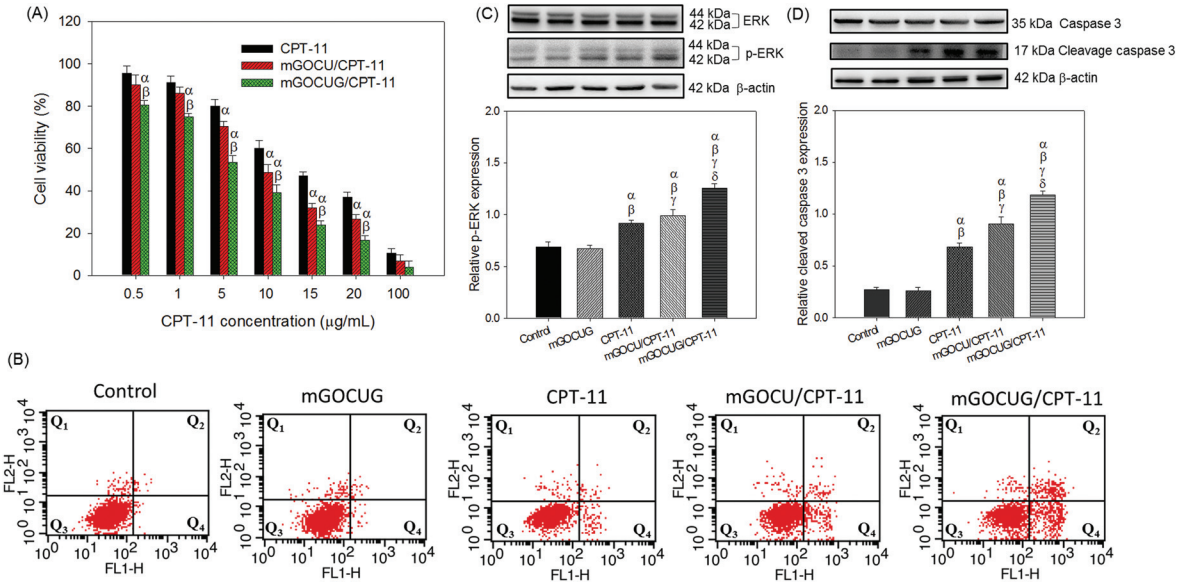

Fig. 10 (A) The cytotoxicity of CPT11, mGOCU/CPT-11 and mGOCUG/CPT-11 toward U87 cells at different concentration in 48 h. $^{\alpha}p < 0.05$ compared with CPT-11; $^{\beta}p < 0.05$ compared with mGOCU/CPT-11. (B) The flow cytometer analysis of the apoptotic and necrotic U87 cells by Annexin V-FITC/PI staining after incubation with different formulations for 24 h. Q_1, necrotic; Q_2, late apoptotic; Q_3, live; Q_4 early apoptotic. (C) The relative expression of phospho-ERK (C) and cleaved caspase 3 (D) apoptosis marker proteins in U87 cells after different treatment was determined by western blotting using β-actin as a loading control. $^{\alpha}p < 0.05$ compared with control; $^{\beta}p < 0.05$ compared with mGOCUG, $^{\gamma}p < 0.05$ compared with CPT-11, $^{\delta}p < 0.05$ compared with mGOCU/CPT-11.

toxicity against U87 cells, as demonstrated from the lowest IC_{50} value in Fig. 10A.

When cancer cells are treated with a chemotherapeutic agent, a signaling pathway involving the extracellular signal-regulated kinases (ERK) protein was activated to produce phospho-ERK (p-ERK) and could result in endoplasmic reticular (ER) stress-induced apoptosis.[67] Furthermore, the activation of caspase 3 to produce cleaved caspase 3 is also a crucial event in cell apoptosis and a reliable indicator.[68] Hence, to evaluate the *in vitro* anticancer mechanism, these apoptosis-related proteins were extracted from U87 cells after subject to various treatments, for western blotting with β-actin as a loading control. As Fig. 10C illustrates, the level of p-ERK protein expression was in the order, control ≅ mGOCUG < CPT-11 < mGOCU/CPT-11 ≪ mGOCUG/CPT-11, with significance between groups as expected. The same trend was also observed with cleaved caspase 3 (Fig. 10D). Taken together, the highest p-ERK and cleaved caspase 3 protein synthesis in U87 cells after treatment with mGOCUG/CPT-11 confirms that the drug-loaded nanocomposite can preferentially enter cancer cells by ligand-mediated endocytosis, after which CPT-11 could be released to induce ER stress and cell apoptosis.

3.7. Antitumor efficacy in the xenograft nude mice animal model

To confirm the bioavailability of mGOCUG to the brain by crossing the BBB and accumulating in the brain tumor region for drug/gene delivery, Cy5.5-labelled mGOCUG/CPT11-shRNA was delivered intravenously *via* the tail vein into U87 brain tumor-bearing mice. Four hours after the administration of the sample, the animal was subject to near infrared fluorescence-based imaging using IVIS (Fig. 11A). When magnetic guidance was introduced by placing a magnet around the brain tumor region after the IV injection of mGOCUG/CPT11/shRNA, a substantial increase of fluorescence intensity was evident from IVIS imaging in the brain area, endorsing the use of magnetic guidance for brain targeting (Fig. 11B).[69] For the quantitative comparison of the distribution of mGOCUG/CPT11/shRNA to the brain, the mice were sacrificed and brain tissues were harvested for *ex vivo* IVIS fluorescence imaging (Fig. 11C). A 6.5-fold increase in fluorescence intensity from 7.9×10^8 to 5.1×10^9 was found when a magnet was used for magnetic guidance after the administration of mGOCUG/CPT11-shRNA intravenously, supporting its use for antitumor treatment in a xenograft nude mice animal model.

The antitumor efficacy of mGOCUG/CPT-11/shRNA under magnetic guidance was then studied *in vivo* in this orthotopic tumor model in nude mice. For this purpose, BALB/c mice (4–5 weeks old, female), with 3×10^5 U87 cells implanted intracranially, were divided into 4 groups ($n = 8$ in each group) and subjected to treatment with normal saline (control), as well as different nanocomposites on day 11 and 14 post-implantation of U87 cells. Bioluminescence imaging (BLI) through IVIS, deemed as a gold standard to monitor the preclinical efficacy of drug candidates in brain tumor therapy,[70] was used to evaluate the treatment efficacy. Fig. 12A reveals the representative IVIS images of tumor-bearing nude mice from different groups on day 12 and 15 post-implantation. In control and

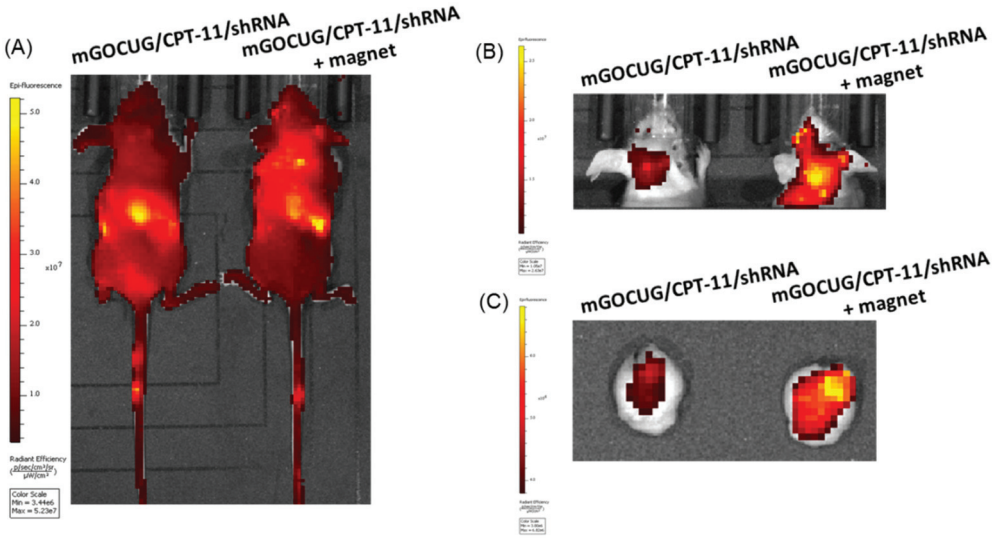

Fig. 11 The whole body (A), brain (B) near infrared fluorescence-based imaging using *in vivo* imaging system (IVIS). The tumor-bearing mouse is injected intravenously with saline (control), Cy5.5-labelled mGOCUG/CPT-11/shRNA or Cy5.5-labelled mGOCUG/CPT-11/shRNA with magnetic guidance by placing a magnet at the brain tumor region. The *ex vivo* images of harvested brains is show in (C).

mGOCUG groups, the BLI signal intensity increased rapidly with time, indicating the vehicle mGOCUG did not possess antitumor efficacy or systemic toxicity to the host. The CPT-11 + shRNA group showed limited suppression ability on tumor growth with the moderate increase of the BLI intensity signal. However, the BLI intensity apparently remained constant in the mGOCUG/CPT-11/shRNA group.

Magnetic resonance imaging (MRI) is considered a gold standard for evaluating the three-dimensional structure and anatomic location of tumor with the advantage of precisely localizing a tumor region or its invasion. Therefore, to investigate whether the antitumor effects obtained from IVIS could correctly reflect the intracranial tumor size, brain MRI was carried out to monitor the tumor size of the same U87 mouse induced with glioblastoma. As shown in Fig. 12B, the time-dependent change of tumor size (circled region) among all groups is consistent with the BLI signals from IVIS. We calculated the volume of the tumor, from three perpendicular diameters of tumor in MRI images as length × width × height/2. The tumor volumes are 966 (or 2281), 558 (or 1172), 758 (or 2257) and 345 (or 541) mm^3 on day 12 (or 15) for control, CPT-11 + shRNA, GOCUG and mGOCUG/CPT-11/shRNA groups, respectively. The control and mGOCUG groups showed a rapid tumor growth rate as expected. On day 15, the tumor size of the CPT11 + shRNA group was 51% of that in the untreated control group. In contrast, the mGOCUG/CPT11/shRNA group exhibited a significantly reduced tumor growth rate, with only 30% of the tumor size in the control group, from dual targeted delivery of mGOCUG/CPT-11/shRNA.

To further investigate the antitumor efficacy quantitatively, all BLI values were standardized to their individual baseline BLI values on day 8, when the randomized grouping of mice was carried out. The normalized BLI intensity is shown for day 12 (Fig. 12C) and day 15 (Fig. 12D). Although the mean value of normalized BLI intensity for the mGOCUG/CPT-11/shRNA group was lower than other groups on day 12, significance was not found on this time point, which was just one day after the first treatment (day 12). Nonetheless, after the second treatment on day 14, the BLI analysis on day 15 clearly indicates that the mGOCUG/CPT-11/shRNA group demonstrates remarkable treatment benefits over other groups with a significantly lower BLI signal intensity. Undoubtedly, the results endorse the antitumor efficacy using mGOCUG as a promising nano-vehicle for the dual targeted delivery of CPT-11 and SLP2 shRNA.

Aside from IVIS, the body weight of mice was closely monitored during the course of treatment to evaluate any adverse effects associated with treatments, with the body weight change normalized with the initial body weight of each mouse on day 8 post-implantation (Fig. 12E). No obvious changes in normalized body weight were noted among all treatment groups with control, indicating no systemic toxicity related to the IV administration of the nanocomposite or the drug-loaded nanocomposite under magnetic guidance. The tumor-bearing mice were sacrificed when they lost more than 20% of the initial body weight, or showing hemiparesis, back hunk and seizures, from where a survival curve can be established form the percentage of remaining mice in each group (Fig. 12F). The median survival times of control, CPT11 + shRNA, and mGOCUG groups were 16.5, 17.5 and 17.5 days, respectively. In contrast, the median survival time extends to 20.5 days in the mGOCUG/CPT-11/shRNA group. As a whole, the survival times are 17.0 ± 3.0, 17.1 ± 2.6, 17.0 ± 2.2 and 22.8 ± 4.1 days (mean ± SD, n = 8) for control, CPT-11 + shRNA, mGOCUG, and mGOCUG/CPT-11/shRNA groups, with the mGOCUG/CPT-11/shRNA treatment showing significantly longer survival time than all other groups ($p < 0.05$).

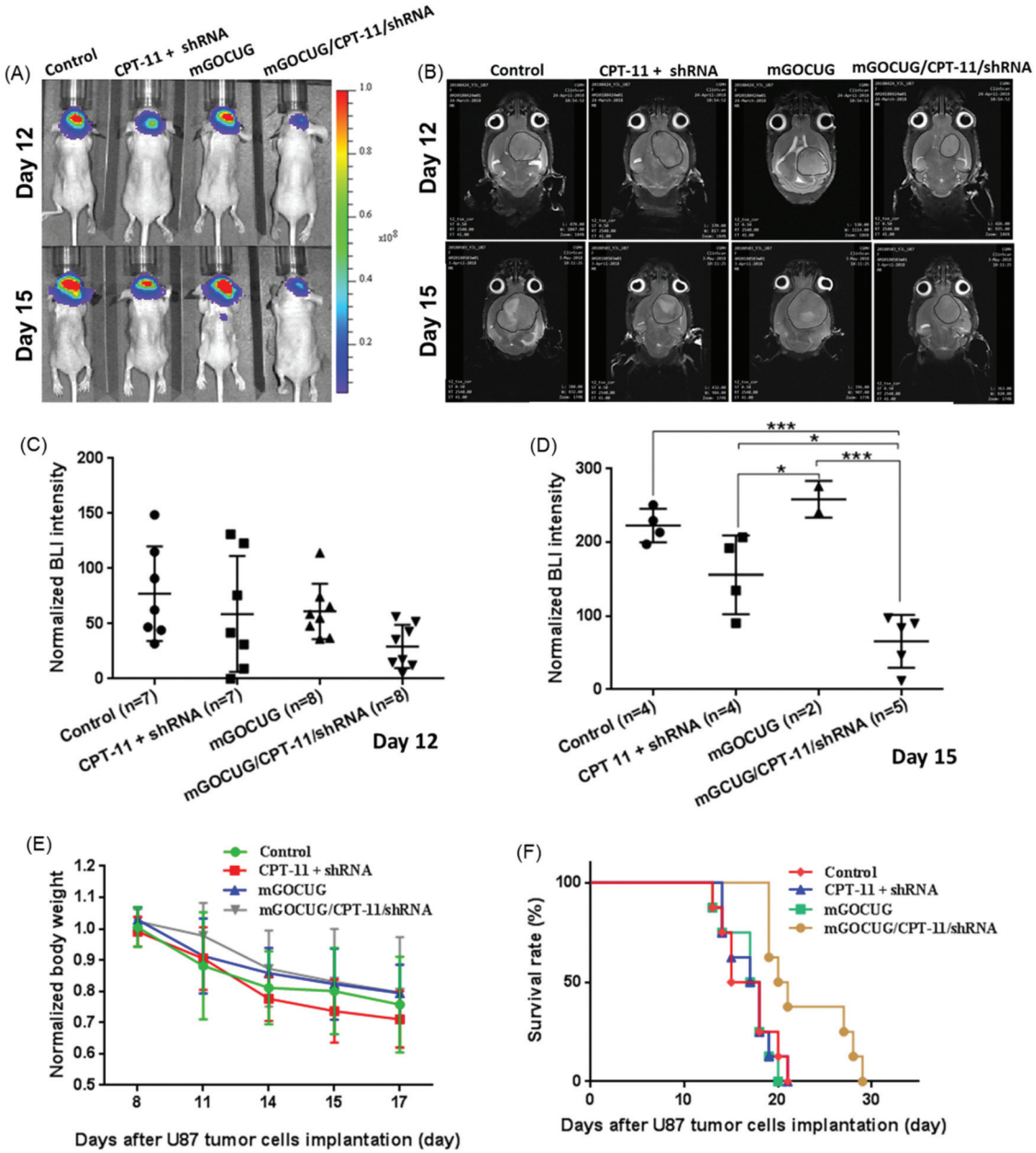

Fig. 12 The antitumor activity induced by the delivery of CPT-11 (7.5 mg kg^{-1}) and SLP2 shRNA (2.5 mg kg^{-1}) to nude mice bearing intracranial U87 tumor. The treatment was carried out by intravenous injection of saline (control) or different formulation on day 11 and 14 post-implantation of U87 cells. The representative images from bioluminescence imaging (BLI) (A), the representative images from magnetic resonance imaging (MRI) (B), and the normalized BLI intensity (relative to grouping on day 8) on day 12 (C) and day 15 (D) post-implantation of U87 cells (*$p < 0.05$, ***$p < 0.005$). The normalized body weights (relative to grouping on day 8) (E) and the survival curves (F) of U87 tumor-bearing mice.

3.8. Histological, immunohistochemical and hematologic analyses

To further evaluate the therapeutic efficiencies from different treatments, sections of tumor samples retrieved on day 18 were subject to histological analysis (Fig. 13A). The H&E staining of tumor tissues collected from the mGOCUG/CPT-11/shRNA group reveals significantly more necrosis regions, more obvious cavitation phenomenon and relatively lower cell density when compared with other groups, indicating vast cell death. In contrast, cell growth without evidence of necrosis is noted in the control and mGOCUG groups. The mGOCUG/CPT-11/shRNA group obviously shows the lowest cell density within all treatment groups, confirming the trend observed from the tumor size with a normalized BLI value. The difference in cell density could be further substantiated from the immunohistochemical (IHC) staining of the Ki-67 protein that has been widely used as a proliferation marker for human

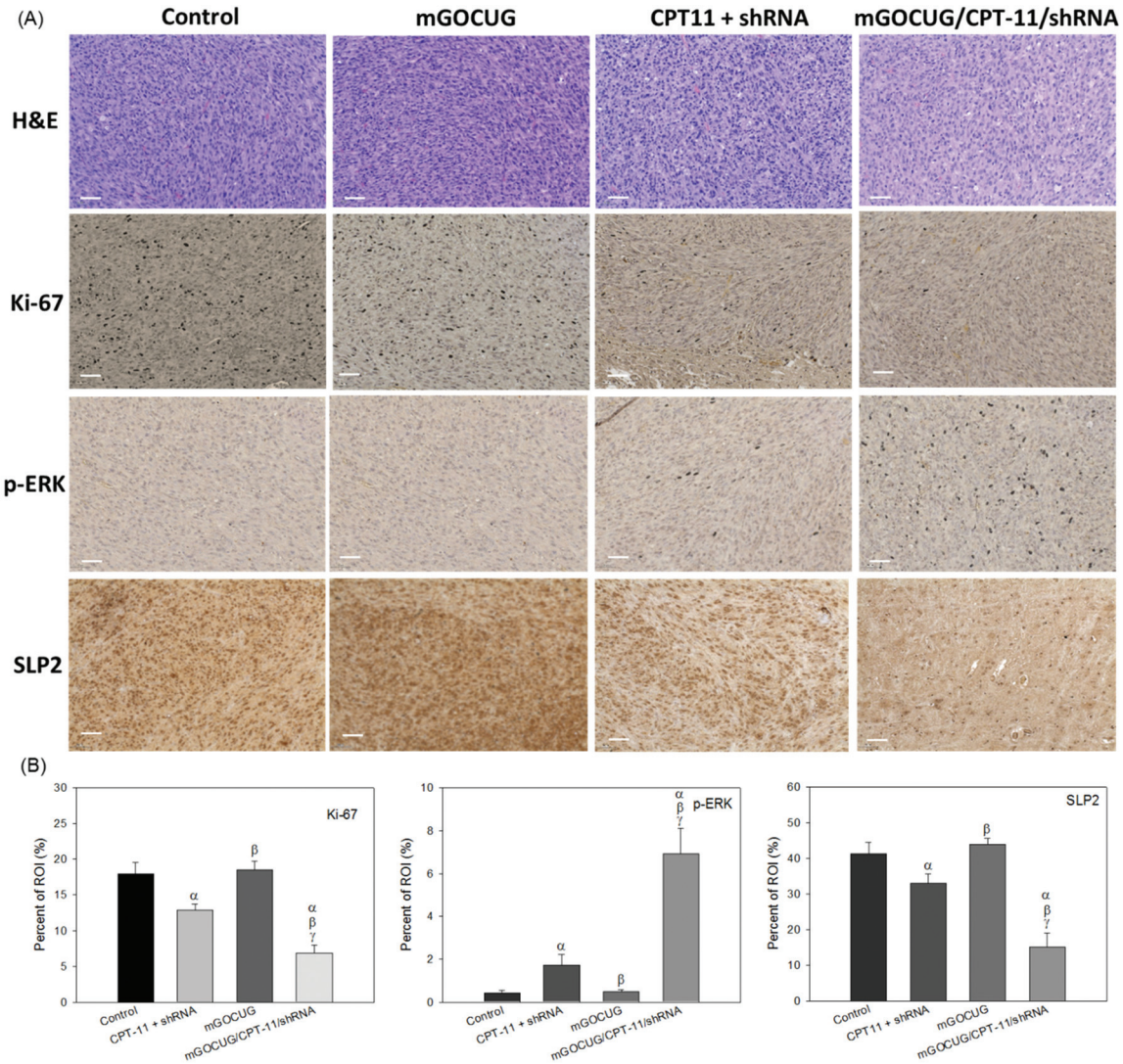

Fig. 13 (A) The H&E staining and immunohistochemical (IHC) staining of Ki-67, p-ERK and SLP2 proteins of tumor tissues in the control group (saline) and groups treated with mGOCUG, CPT-11 + shRNA or mGOCUG/CPT-11/shRNA on day 18 after post-implantation of U87 cells (bar = 50 μm). (B) The quantitative analysis of Ki-67, p-ERK, and SLP2 from IHC staining by calculating the area percentage of the immune-reactive area within the region of interest (ROI). $^{\alpha}p < 0.05$ compared with control, $^{\beta}p < 0.05$ compared with CPT-11 + shRNA, $^{\gamma}p < 0.05$ compared with mGOCUG.

tumor cells.[71] The control and mGOCUG groups displayed high immunoreactivity from actively proliferating U87 cells, while the tumor treated with mGOCUG/CPT-11/shRNA shows weak Ki-67 immunoreactivity (Fig. 13A). Although the tumor section from mice treated with CPT-11 + shRNA shows less Ki-67 secreting cells, the mGOCUG/CPT-11/shRNA group leads to minimum Ki-67 production, possibly from the pronounced apoptosis of U87 cells. This group also reveals the significantly reduced percentage of the Ki-67 stained area in the ROI from other groups, indicating the most effective anti-glioblastoma efficacy *in vivo* (Fig. 13B).

The trend noted in both H&E and Ki-67 staining could be further supported from IHC staining of a biomarker phospho-ERK (p-ERK) protein in the tumor tissue, which is a reliable indicator of cell apoptosis caused by CPT-11 (Fig. 13A).[69] The control and mGOCUG groups show close to zero pERK-stained area and some p-ERK production is noted for the CPT-11 + shRNA group (Fig. 13B). The result revealed the most intense expression of the p-ERK protein in the tumor tissue section of mGOCUG/CPT-11/shRNA-treated mice, consistent with the *in vitro* western blot analysis (Fig. 10C). The mean percent ROI value for p-ERK increases significantly from 1.7% for CPT-11 + shRNA to 6.9% for mGOCUG/CPT-11/shRNA. Additionally, the mGOCUG/CPT-11/shRNA group also demonstrates significantly less SLP2 protein expression, after gene knockdown *via* the efficient delivery of SLP2 shRNA, confirming successful RNAi therapeutics *in vivo* (Fig. 13A). The means of the percentage of the positively stained area for SLP2 in the ROI are 41.3%, 33.0%, 43.9%, and 15.2% for mice treated with normal saline, CPT-11 + shRNA, mGOCUG, and mGOCUG/CPT-11/

Table 2 Hematological values (mean ± SD, n = 3) of treated mice

Item	Unit	Control	CPT-11 + shRNA	mGOCUG	mGOCUG/CPT-11/shRNA
WBC	10^3 per μL	3.63 ± 1.11	2.92 ± 0.73	2.79 ± 1.07	3.63 ± 1.45
RBC	10^6 per μL	7.57 ± 0.21	8.27 ± 0.15	7.77 ± 0.36	8.79 ± 0.65
HGB	g dL^{-1}	12.87 ± 0.37	13.63 ± 0.17	13.23 ± 0.50	14.63 ± 0.73
HCT	%	43.10 ± 0.60	44.33 ± 0.69	42.17 ± 2.10	47.82 ± 1.34
MCV	fL	57.04 ± 1.81	53.57 ± 0.93	54.27 ± 0.88	54.53 ± 2.85
MCH	pg	17.23 ± 0.22	16.47 ± 0.39	17.65 ± 0.33	16.63 ± 0.46
MCHC	g dL^{-1}	29.83 ± 0.73	30.77 ± 0.19	31.43 ± 1.01	30.57 ± 0.88
PLT	10^3 per μL	480.3 ± 55.7	520.1 ± 90.1	528.7 ± 94.1	482.6 ± 58.9

WBC, white blood cell; RBC, red blood cell; HGB, hemoglobin; HCT, hematocrit; MCV, mean corpuscular volume; MCH, mean corpuscular hemoglobin; MCHC: mean corpuscular hemoglobin concentration; PLT, platelet.

shRNA, respectively (Fig. 13B). Taken together, these results demonstrate enhanced antitumor efficacy of mGOCUG/CPT-11/shRNA through dual targeted delivery of CPT-11 and shRNA, which can provide an excellent treatment modality for glioblastoma therapy from orthotopic brain tumor model created with U87 xenografts.

The hematologic analyses of sacrificed mice were performed to compare the potential toxicities from the treatments with the control group. As shown in Table 2, the application of CPT-11 + shRNA, mGOCUG and mGOCUG/CPT-11/shRNA did not significantly alter the level of blood counts when compared with the control group, consistent with the result of body weight change shown before. Hence, the co-delivery of CPT-11 and shRNA by mGOCUG will not cause remarkable adverse effects from hematological analysis, which has been a prerequisite in nanomedicine for drug delivery.

4. Conclusion

We aim to develop a dual-targeted drug/gene delivery nanovehicle based on a GO derivative for the co-delivery of CPT-11 and SLP2 shRNA in the treatment of invasive brain gliomas. For this purpose, we successfully prepared mGO *via* chemical co-precipitation of Fe_3O_4 MNPs on the GO surface, which can be precisely navigated to tumors using an external magnetic field as well as equipped with a targeting ligand to facilitate endocytosis for maximal therapeutic efficacy. As for the targeting efficacy, mGOCUG/CPT11 showed a 4.9-fold increase in drug uptake efficacy when compared with free CPT-11 *in vitro*. *In vivo* brain tumor targeting indicates that magnetic guidance can enhance the ability of mGOCUG/CPT-11/shRNA to cross the BBB by 6.5 fold. This formulation showed pH-responsive drug release behavior to enable the controllable release of the loaded chemo drug CPT-11 in the endosomes after intracellular uptake, as well as the endosomal escape ability to provide effective gene silencing from SLP2 shRNA delivery. mGOCUG/CPT-11/shRNA demonstrates excellent antitumor efficacy in a xenograft nude mouse animal model bearing an orthotopic tumor in the brain, by remarkably reducing the tumor growth rate and prolonging the animal survival time. Moreover, the tumor-bearing mice revealed a similar body weight change and hematologic parameters to the control group after treatment, indicating a highly compatible tumor treatment modality. Overall, this drug/gene delivery platform is suitable for treating glioblastoma with an enhanced therapeutic efficacy and minimal adverse effects.

Conflicts of interest

There are no conflicts to declare.

Acknowledgements

The authors would like to thank the Ministry of Science and Technology of Taiwan (ROC) (MOST106-2221-E-182-056-MY3) and Chang Gung Memorial Hospital (CMRPD2L0101) for financial support. We acknowledge the technical support by the Microscopy Center and Instrumentation Center, Chang Gung University, and the Imaging Core Laboratories of the Institute for Radiological Research, Chang Gung Memorial Hospital.

References

1 M. Koshy, J. L. Villano, T. A. Dolecek, A. Howard, U. Mahmood, S. J. Chmura, R. R. Weichselbaum and B. J. McCarthy, *J. Neurooncol.*, 2012, **107**, 207–212.
2 Q. T. Ostrom, G. Cioffi, H. Gittleman, N. Patil, K. Waite, C. Kruchko and J. S. Barnholtz-Sloan, *Neuro-Oncol.*, 2019, **21**, v1–v100.
3 T. J. Brown, M. C. Brennan, M. Li, E. W. Church, N. J. Brandmeir, K. L. Rakszawski, A. S. Patel, E. B. Rizk, D. Suki, R. Sawaya and M. Glantz, *JAMA Oncol.*, 2016, **2**, 1460–1469.
4 Y. M. Li, D. Suki, K. Hess and R. Sawaya, *J. Neurosurg.*, 2016, **124**, 977–988.
5 N. A. Charles, E. C. Holland, R. Gilbertson, R. Glass and H. Kettenmann, *Glia*, 2012, **60**, 502–514.
6 A. Shergalis, A. Bankhead 3rd, U. Luesakul, N. Muangsin and N. Neamati, *Pharmacol. Rev.*, 2018, **70**, 412–445.

7 H. S. Friedman, M. D. Prados, P. Y. Wen, T. Mikkelsen, D. Schiff, L. E. Abrey, W. K. Yung, N. Paleologos, M. K. Nicholas, R. Jensen, J. Vredenburgh, J. Huang, M. Zheng and T. Cloughesy, *J. Clin. Oncol.*, 2009, **27**, 4733–4740.
8 M. D. Prados, K. Lamborn, W. K. Yung, K. Jaeckle, H. I. Robins, M. Mehta, H. A. Fine, P. Y. Wen, T. Cloughesy, S. Chang, M. K. Nicholas, D. Schiff, H. Greenberg, L. Junck, K. Fink, K. Hess and J. Kuhn, *Neuro-Oncol.*, 2006, **8**, 189–193.
9 N. Karra and S. Benita, *Curr. Drug Metab.*, 2012, **13**, 22–41.
10 S. Senapati, A. K. Mahanta, S. Kumar and P. Maiti, *Signal Transduction Targeted Ther.*, 2018, **3**, 7.
11 F. Yuan, M. Dellian, D. Fukumura, M. Leunig, D. A. Berk, V. P. Torchilin and R. K. Jain, *Cancer Res.*, 1995, **55**, 3752–3756.
12 T. M. Allen and P. R. Cullis, *Science*, 2004, **303**, 1818–1822.
13 J. Liu, L. Cui and D. Losic, *Acta Biomater.*, 2013, **9**, 9243–9257.
14 X. Yang, X. Zhang, Z. Liu, Y. Ma, Y. Huang and Y. Chen, *J. Phys. Chem. C*, 2008, **112**, 17554–17558.
15 Y.-S. Huang, Y.-J. Lu and J.-P. Chen, *J. Magn. Magn. Mater.*, 2017, **427**, 34–40.
16 T. A. Tabish and R. J. Narayan, *Mater. Today*, 2021, **51**, 393–401.
17 K. Nguyen, P. N. Dang and E. Alsberg, *Acta Biomater.*, 2013, **9**, 4487–4495.
18 Y. J. Lu, P. Y. Lin, P. H. Huang, C. Y. Kuo, K. T. Shalumon, M. Y. Chen and J. P. Chen, *Nanomaterials*, 2018, **8**, 193.
19 L. Shen, B. Li and Y. Qiao, *Materials*, 2018, **11**, 324.
20 H. W. Yang, M. Y. Hua, T. L. Hwang, K. J. Lin, C. Y. Huang, R. Y. Tsai, C. C. Ma, P. H. Hsu, S. P. Wey, P. W. Hsu, P. Y. Chen, Y. C. Huang, Y. J. Lu, T. C. Yen, L. Y. Feng, C. W. Lin, H. L. Liu and K. C. Wei, *Adv. Mater.*, 2013, **25**, 3605–3611.
21 C.-Y. Chiu, T.-W. Chung, S.-Y. Chen and Y.-H. Ma, *Int. J. Nanomed.*, 2019, **14**, 4767–4780.
22 M. F. Attia, N. Anton, J. Wallyn, Z. Omran and T. F. Vandamme, *J. Pharm. Pharmacol.*, 2019, **71**, 1185–1198.
23 H. Kiaris, A. V. Schally, B. Sun, P. Armatis and K. Groot, *Oncogene*, 1999, **18**, 7168–7173.
24 J. Mattei, R. D. Achcar, C. H. Cano, B. R. Macedo, L. Meurer, B. S. Batlle, S. D. Groshong, J. M. Kulczynski, R. Roesler, L. Dal Lago, A. T. Brunetto and G. Schwartsmann, *Arch. Pathol. Lab. Med.*, 2014, **138**, 98–104.
25 D. B. Cornelio, L. Meurer, R. Roesler and G. Schwartsmann, *Oncology*, 2007, **73**, 340–345.
26 J. Zhou, J. Chen, M. Mokotoff and E. D. Ball, *Anticancer Drugs*, 2004, **15**, 921–927.
27 S. R. Preston, L. F. Woodhouse, S. Jones-Blackett, G. V. Miller and J. N. Primrose, *Br. J. Cancer*, 1995, **71**, 1087–1089.
28 C. Morgat, G. MacGrogan, V. Brouste, V. Vélasco, N. Sévenet, H. Bonnefoi, P. Fernandez, M. Debled and E. Hindié, *J. Nucl. Med.*, 2017, **58**, 1401–1407.
29 J. C. Reubi, S. Wenger, J. Schmuckli-Maurer, J. C. Schaer and M. Gugger, *Clin. Cancer Res.*, 2002, **8**, 1139–1146.
30 D. G. Flores, L. Meurer, A. F. Uberti, B. R. Macedo, G. Lenz, A. L. Brunetto, G. Schwartsmann and R. Roesler, *Brain Res. Bull.*, 2010, **82**, 95–98.
31 M. K. Yu, J. Park and S. Jon, *Theranostics*, 2012, **2**, 3–44.
32 S. Lakkadwala, B. Dos Santos Rodrigues, C. Sun and J. Singh, *J. Controlled Release*, 2019, **307**, 247–260.
33 W. Wang, H. Song, J. Zhang, P. Li, C. Li, C. Wang, D. Kong and Q. Zhao, *J. Controlled Release*, 2015, **203**, 57–66.
34 X. Dai and C. Tan, *Adv. Drug Delivery Rev.*, 2015, **81**, 184–197.
35 D. D. Guo, S. H. Hong, H. L. Jiang, J. H. Kim, A. Minai-Tehrani, J. E. Kim, J. Y. Shin, T. Jiang, Y. K. Kim, Y. J. Choi, C. S. Cho and M. H. Cho, *Biomaterials*, 2012, **33**, 2272–2281.
36 H. Ma, C. He, Y. Cheng, D. Li, Y. Gong, J. Liu, H. Tian and X. Chen, *Biomaterials*, 2014, **35**, 8723–8734.
37 P. Y. Teo, W. Cheng, J. L. Hedrick and Y. Y. Yang, *Adv. Drug Delivery Rev.*, 2016, **98**, 41–63.
38 K. L. Kozielski, A. Ruiz-Valls, S. Y. Tzeng, H. Guerrero-Cázares, Y. Rui, Y. Li, H. J. Vaughan, M. Gionet-Gonzales, C. Vantucci, J. Kim, P. Schiapparelli, R. Al-Kharboosh, A. Quiñones-Hinojosa and J. J. Green, *Biomaterials*, 2019, **209**, 79–87.
39 Y. Xia, J. Tian and X. Chen, *Biomaterials*, 2016, **79**, 56–68.
40 W. E. Rudzinski and T. M. Aminabhavi, *Int. J. Pharm.*, 2010, **399**, 1–11.
41 H. Ragelle, G. Vandermeulen and V. Préat, *J. Controlled Release*, 2013, **172**, 207–218.
42 A. Afkham, L. Aghebati-Maleki, H. Siahmansouri, S. Sadreddini, M. Ahmadi, S. Dolati, N. M. Afkham, P. Akbarzadeh, F. Jadidi-Niaragh, V. Younesi and M. Yousefi, *Pharmacol. Rep.*, 2018, **70**, 418–425.
43 M. Alameh, M. Lavertu, N. Tran-Khanh, C.-Y. Chang, F. Lesage, M. Bail, V. Darras, A. Chevrier and M. D. Buschmann, *Biomacromolecules*, 2018, **19**, 112–131.
44 S. Mao, W. Sun and T. Kissel, *Adv. Drug Delivery Rev.*, 2010, **62**, 12–27.
45 Y. Cao, Y. F. Tan, Y. S. Wong, M. W. J. Liew and S. Venkatraman, *Mar. Drugs*, 2019, **17**, 381.
46 T. H. Kim, J. E. Ihm, Y. J. Choi, J. W. Nah and C. S. Cho, *J. Controlled Release*, 2003, **93**, 389–402.
47 L. Han, C. Tang and C. Yin, *Biomaterials*, 2015, **44**, 111–121.
48 L. Song, L. Liu, Z. Wu, C. Lin, T. Dai, C. Yu, X. Wang, J. Wu, M. Li and J. Li, *J. Pathol.*, 2012, **226**, 534–543.
49 L. Zhang, F. Ding, W. Cao, Z. Liu, W. Liu, Z. Yu, Y. Wu, W. Li, Y. Li and Z. Liu, *Clin. Cancer Res.*, 2006, **12**, 1639–1646.
50 D. Chang, K. Ma, M. Gong, Y. Cui, Z. H. Liu, X. G. Zhou, C. N. Zhou and T. Y. Wang, *Biomarkers*, 2010, **15**, 104–110.
51 B. Wang, J. Xie, H.-Y. He, E.-W. Huang, Q.-H. Cao, L. Luo, Y.-S. Liao and Y. Guo, *Oncotarget*, 2017, **8**, 63788–63798.
52 X. Sun, Z. Liu, K. Welsher, J. T. Robinson, A. Goodwin, S. Zaric and H. Dai, *Nano Res.*, 2008, **1**, 203–212.
53 B. S. Dash, Y.-J. Lu, H.-A. Chen, C.-C. Chuang and J.-P. Chen, *Mater. Sci. Eng., C*, 2021, **128**, 112311.

54 S.-i. Kojima, D. Vignjevic and G. G. Borisy, *BioTechniques*, 2004, **36**, 74–79.
55 M. Danaei, M. Dehghankhold, S. Ataei, F. Hasanzadeh Davarani, R. Javanmard, A. Dokhani, S. Khorasani and M. R. Mozafari, *Pharmaceutics*, 2018, **10**, 57.
56 S. Perumbilavil, P. Sankar, T. Priya Rose and R. Philip, *Appl. Phys. Lett.*, 2015, **107**, 051104.
57 N. H. Kim, T. Kuila and J. H. Lee, *J. Mater. Chem. A*, 2013, **1**, 1349–1358.
58 R.-P. Liang, C.-M. Liu, X.-Y. Meng, J.-W. Wang and J.-D. Qiu, *J. Chromatogr. A*, 2012, **1266**, 95–102.
59 J. Shen, M. Shi, H. Ma, B. Yan, N. Li and M. Ye, *Mater. Res. Bull.*, 2011, **46**, 2077–2083.
60 L. Q. Xu, L. Wang, B. Zhang, C. H. Lim, Y. Chen, K.-G. Neoh, E.-T. Kang and G. D. Fu, *Polymer*, 2011, **52**, 2376–2383.
61 S. Ghosh, A. Z. M. Badruddoza, K. Hidajat and M. S. Uddin, *J. Environ. Chem. Eng.*, 2013, **1**, 122–130.
62 J. P. Chen, P. C. Yang, Y. H. Ma, S. J. Tu and Y. J. Lu, *Int. J. Nanomed.*, 2012, **7**, 5137–5149.
63 Wahajuddin and S. Arora, *Int. J. Nanomed.*, 2012, **7**, 3445–3471.
64 Q. Lin, K. L. Mao, F. R. Tian, J. J. Yang, P. P. Chen, J. Xu, Z. L. Fan, Y. P. Zhao, W. F. Li, L. Zheng, Y. Z. Zhao and C. T. Lu, *Cancer Chemother. Pharmacol.*, 2016, **77**, 269–280.
65 D. Peng, Z. Fan, Y. Lu, T. DeBlasio, H. Scher and J. Mendelsohn, *Cancer Res.*, 1996, **56**, 3666–3669.
66 B. Xiao, P. Ma, E. Viennois and D. Merlin, *Colloids Surf., B*, 2016, **143**, 186–193.
67 K. Arai, S. R. Lee, K. van Leyen, H. Kurose and E. H. Lo, *J. Neurochem.*, 2004, **89**, 232–239.
68 A. G. Porter and R. U. Jänicke, *Cell Death Differ.*, 1999, **6**, 99–104.
69 Y.-J. Lu, E.-Y. Chuang, Y.-H. Cheng, T. S. Anilkumar, H.-A. Chen and J.-P. Chen, *Chem. Eng. J.*, 2019, **373**, 720–733.
70 S. C. Jost, L. Collins, S. Travers, D. Piwnica-Worms and J. R. Garbow, *Mol. Imaging*, 2009, **8**, 245–253.
71 X. Sun and P. D. Kaufman, *Chromosoma*, 2018, **127**, 175–186.

